


Appropriate Mechanical Confinement Inhibits Multipolar Cell Division via Pole-Cortex Interaction

Longcan Cheng¹,* Jingchen Li¹,* Houbo Sun¹, and Hongyuan Jiang¹†

CAS Key Laboratory of Mechanical Behavior and Design of Materials,
CAS Center for Excellence in Complex System Mechanics, Department of Modern Mechanics,
University of Science and Technology of China, Hefei, Anhui 230026, China

 (Received 15 March 2022; revised 30 November 2022; accepted 26 January 2023; published 10 March 2023)

Multipolar spindles are very rare in normal tissues, but they are much more prevalent in many tumors, which might be induced by the mechanical confinements from overcrowding microenvironments in tumors. However, little is known about what the difference is between various forms of mechanical confinements that cells encounter in normal tissues and tumor tissues, and how they affect multipolarity and chromosome segregation fidelity. Here, we use microchannels with different heights and widths to mimic diverse forms and degrees of mechanical constraints within the tissue architecture. We find that multipolar spindles occur frequently under two-wall confinement but that they are rare under four-wall confinement, suggesting that multipolar-spindle assembly depends on the form of the three-dimensional mechanical confinement. We reveal that two-wall confinement leads to an increased fraction of multipolar spindles by pole splitting, while four-wall confinement restrains multipolarity by the enhancement of pole clustering and the inhibition of pole splitting. We further conduct numerical simulations and develop a theoretical model to investigate how mechanical confinement influences pole splitting and clustering. By exploring the energy landscape of pole-pole interactions and pole-cortex interactions and treating pole splitting and clustering as reversible reactions, we demonstrate that mechanical confinement controls cell shape and pole-cortex interactions, which, in turn, change the energy barriers of pole splitting and clustering as well as the probability of multipolar mitosis. Further experiments confirm the theoretical prediction that the pole-cortex interaction determines the probability of the multipolar spindles under various mechanical confinements. Our findings demonstrate the extent to which extracellular microenvironments and tissue architecture can affect complex cellular behaviors, indicating that normal tissue architecture may have the ability to suppress the progress of cancers. Thus, our findings would provide essential cues for cancer therapies targeting the tumor microenvironment.

DOI: [10.1103/PhysRevX.13.011036](https://doi.org/10.1103/PhysRevX.13.011036)

Subject Areas: Biological Physics,
Interdisciplinary Physics

I. INTRODUCTION

A remarkable feature of many cancer cells is the higher rate of gain or loss of whole chromosomes, a phenomenon termed chromosome instability (CIN) [1–5]. One of the major causes of CIN are multipolar spindles, which are prevalent in many human cancer cells [4,6] and polyploid cells such as regenerating adult hepatocytes [5,7,8]. The presence of multipolar spindles is associated with supernumerary centrosomes due to centrosome overduplication

or cytokinesis failure [9,10], and the loss of spindle pole integrity [11–13], including premature centriole disengagement and pericentriolar material (PCM) fragmentation [6]. To ensure the chromosome segregation fidelity into the two daughter cells, cells subjected to multipolar spindles will initiate a correction mechanism by clustering supernumerary or fragmented centrosomes into a functional bipolar spindle [2,4,14–18].

Most of our current understanding about the behaviors of multipolar spindles, including pole splitting and pole clustering, comes from *in vitro* culture systems, but little is known about the influence of sophisticated tissue architecture. Actually, cells *in vivo* suffer from mechanical confinement from adjacent cells and extracellular matrices, so their shape, adhesion, and mitosis are intrinsically different from the *in vitro* culture environment. From the *in vivo* tissue to the *in vitro* environment, there is a risk of removing too much context and therefore sacrificing the mechanical or

*These two authors contributed equally to this work.

†jianghy@ustc.edu.cn

Published by the American Physical Society under the terms of the [Creative Commons Attribution 4.0 International license](https://creativecommons.org/licenses/by/4.0/). Further distribution of this work must maintain attribution to the author(s) and the published article's title, journal citation, and DOI.

geometrical constraints that guide the behavior of the cellular system [19]. To solve this problem, *in vitro* experiments have begun to focus on faithfully recapitulating extracellular constraints, known as “boundary conditions” in physics [19], and to investigate how an extracellular mechanical microenvironment regulates various cellular behaviors [20–27]. However, how the mechanical confinements from extracellular microenvironments influence the behaviors of multipolar spindles still remains unclear.

Recent studies have suggested that mechanical confinement from normal tissue architecture can ensure chromosome segregation fidelity. For example, chromosome segregation defects are never observed in epithelial cells within the tissue of mammary glands, embryonic skin, and neonatal liver [8]. However, when these epithelial cells are dissociated from their native tissue and cultured on a 2D surface, the appearance of lagging chromosomes and micronuclei significantly increases [8]. Consistently, the results of single-cell sequencing of hepatocytes, both in mice and humans, highlight the rarity of aneuploidy across tissue scales [8,28], but hepatocytes *in vitro* culture exhibit high frequencies of chromosome segregation defects and aneuploidy [5,7,8]. Moreover, within the context of a developing organism, the tissue architecture can facilitate the pole clustering of *Drosophila* somatic cells with extra centrosomes [15]. These results strongly suggest that the mechanical constraints from surrounding normal tissue can rescue multipolar mitosis and chromosome segregation defects [8,15].

Compared to normal tissues, many tumor tissues display much more multipolar mitosis [4,6], which may be induced by the highly crowded three-dimensional microenvironment that cancer cells encounter *in vivo* [29,30]. Uncontrolled proliferation of cancer cells *in vivo* generates compressive mechanical stress within tumors [29,30], and the stress accumulated during tumor growth makes cancer cells densely packed [29,30] and even collapses blood and lymphatic vessels within the tumor [31]. The crowding environment, e.g., severe height confinement, can result in the fragmentation and splitting of the spindle pole, so the probability of multipolar spindles and multidaughter cell division remarkably increases [32–34]. The significant difference between normal tissues and tumor tissues indicates that multipolar cell division is very sensitive to the mechanical constraints from an extracellular microenvironment. However, the difference between various forms of mechanical confinement that cells encounter in normal tissues and tumor tissues, and how they affect multipolarity and chromosome segregation fidelity still remain elusive.

To answer these questions, we use microchannels with various heights and widths to confine cells so that the form and degree of mechanical confinement can be well controlled. Surprisingly, our results show that two-wall confinement promotes multipolar spindles by increasing the pole splitting, while four-wall confinement restrains

multipolarity by the enhancement of pole clustering and the inhibition of pole splitting. Combining experiments with numerical simulation and a theoretical model, we treat pole splitting and clustering as reversible reactions and demonstrate that mechanical confinement controls cell shape and pole-cortex interactions, which, in turn, change the energy barriers of pole splitting and clustering as well as the probability of multipolar mitosis. Our results highlight that the extracellular mechanical microenvironment matters, and our findings provide a biophysical understanding and basis for potential cancer therapies by modifying the tumor microenvironment to suppress tumor progression.

II. RESULTS

A. Frequent multipolar mitosis under two-wall confinement and rare multipolar mitosis under four-wall confinement

To mimic various forms of mechanical confinement, especially the mechanical confinement of epithelial tissue architecture [Fig. 1(a)], we fabricate microchannels with various heights (H) and widths (W) from polydimethylsiloxane (PDMS) by means of a photolithographic protocol [35–37] [Fig. 1(b)]. We choose HeLa cells since they are recognized as CIN cells harboring multipolar spindles [4]. The average volume of HeLa cells is about $3300 \mu\text{m}^3$ [Figs. 1(c) and S1 [38]]. Based on this value, we propose a phase diagram to distinguish the level of mechanical confinement during mitosis [Fig. 1(d); more details can be found in Appendix A 6]. The phase diagram contains three regions, i.e., no confinement (cell rounding freely during mitosis), two-wall confinement (only cell height or cell width is confined during mitosis), and four-wall confinement (both cell height and width are confined) [Fig. 1(d)]. The diagram displays the reflection symmetry about the line $H = W$ due to the intrinsic symmetry of the height and width of microchannels. In the case of two-wall confinement, only the cell height is confined in our experiments [32–34] since it is inconvenient to confine cells and observe the spindles through the microscope when the cell width is confined.

In accordance with previously works [32,39], we find that about 12% of free HeLa cells (with no confinement) can exhibit multipolar spindles, with three, four, five, or even more poles [Figs. 1(f) and S2]. Furthermore, we observe a much higher frequency of multipolar spindles under the various levels of two-wall confinement ($5 \mu\text{m}$, $H = 3$), and $7 \mu\text{m}$) in comparison with free cells, and the frequency increases to 60% as the channel height decreases to $3 \mu\text{m}$ [Figs. 1(h), 1(g), and S3], which is consistent with the previous studies [32–34]. We find that $10 \mu\text{m}$ is a critical height, below which spindle deformations will induce a higher frequency of multipolar spindles.

To study the impact of four-wall confinement and exclude the influence of two-wall confinement, we fix

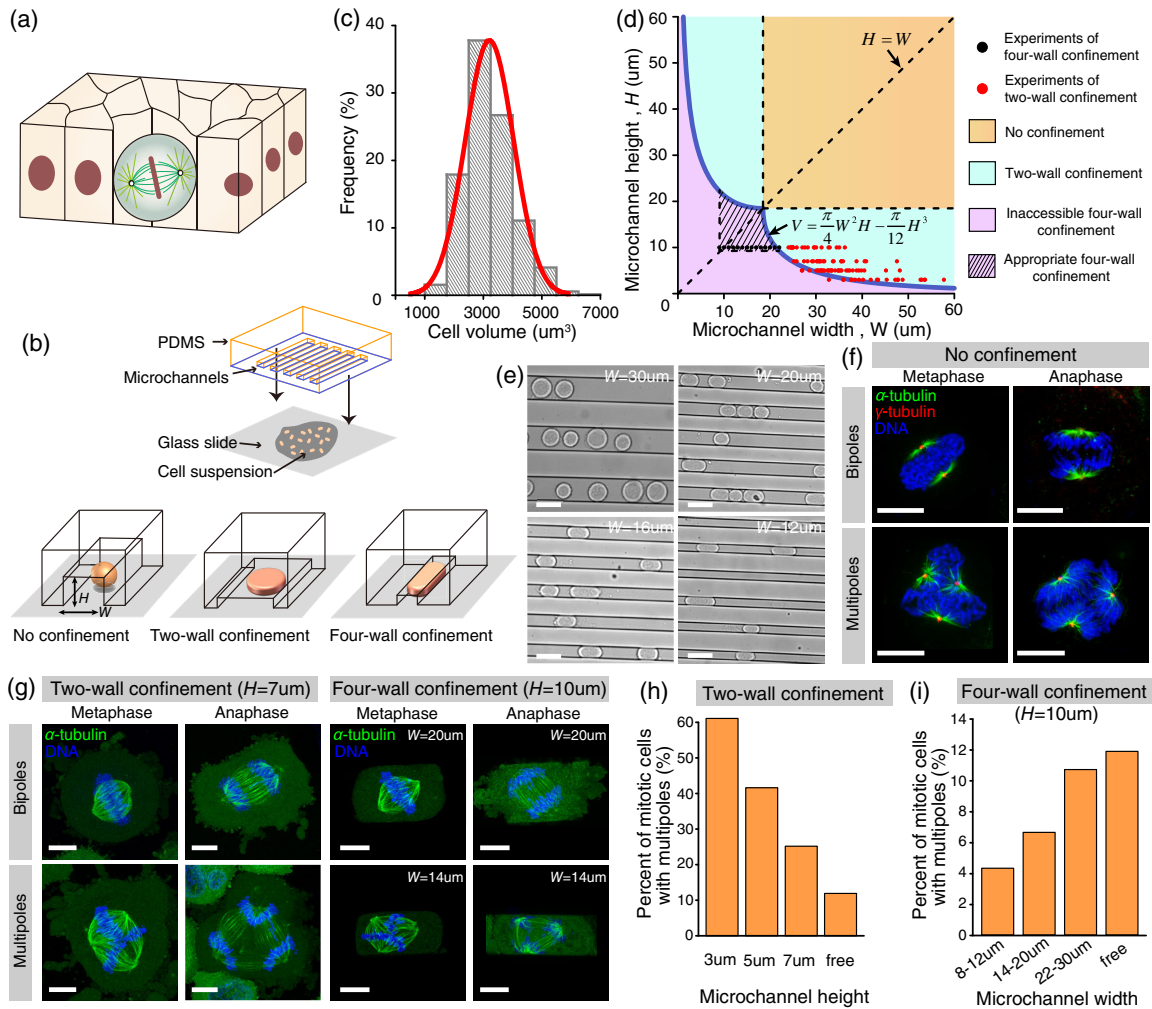


FIG. 1. Frequent multipolar mitosis under two-wall confinement and rare multipolar mitosis under four-wall confinement. (a) Schematic diagram of the mechanical confinement from epithelial tissue architecture during mitosis. (b) Schematic diagram of mitotic cells under no confinement, two-wall confinement, and four-wall confinement. (c) Distribution of cell volume of HeLa cells. (d) Phase diagram of the level of mechanical confinement to mitotic cells. (e) Bright field images of cells in microchannels with $H = 10 \mu\text{m}$ and various widths. The scale bar is $30 \mu\text{m}$. (f,g) Images of metaphase and anaphase HeLa cells under no confinement (fixed cells), $7 \mu\text{m}$ height confinement (living cells), and four-wall confinement (living cells) with stained α tubulin (green), γ tubulin (red), and DNA (blue). The scale bar is $10 \mu\text{m}$. (h,i) Percentage of multipolar mitosis in all mitotic cells in free culture ($n = 1210$), two-wall ($n = 756, 1060, 719$), and four-wall confinement ($n = 372, 556, 659$).

the channel height at $10 \mu\text{m}$ and change the channel width from 8 to $30 \mu\text{m}$ [Fig. 1(e)]. Strikingly, we find that the frequency of multipolar spindles under four-wall confinement is much lower compared with free cells, and the frequency decreases to 4% as the channel width decreases to $8\text{--}12 \mu\text{m}$ [Figs. 1(i) and S3], which is totally different from the results of two-wall confinement [Figs. 1(h) and S3]. A similar phenomenon is also observed in MDA-MB-231 cells (Fig. S3). These observations lead to a surprising conclusion that multipolar spindles are frequent under two-wall confinement but rare under four-wall confinement, suggesting that multipolar-spindle assembly depends on the architecture of the three-dimensional mechanical confinement.

B. Two-wall confinement leading to more multipolar spindles by increasing pole splitting; four-wall confinement restraining multipolar spindles by inhibiting splitting and the enhancement of clustering

To resolve the paradox, we record and analyze the entire process of mitosis from the nuclear envelope breakdown (NEB) to telophase or cell death [Figs. 2(a) and 2(b)]. We find that some multipolar spindles are naturally assembled with constant pole numbers throughout the mitosis (Fig. S4 and movie S1 in Supplemental Material [38]), which is referred to as “maintain.” Many more multipolar spindles are induced by the pole splitting, i.e., the transition from one pole to two poles [Fig. 2(a) and movie S1 [38]]. Notice that the number of spindle poles is based on the puncta of α

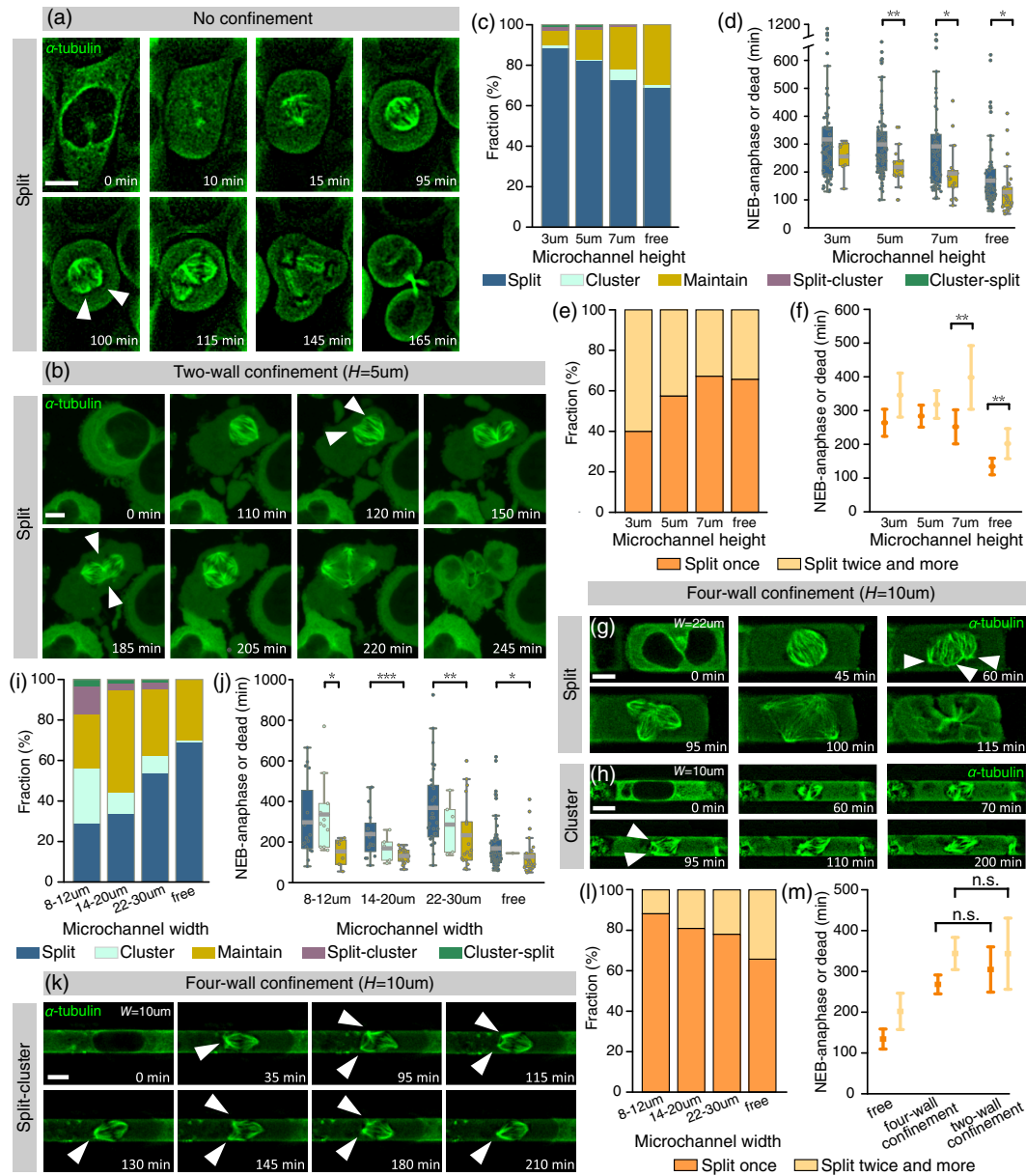


FIG. 2. Two-wall confinement leading to more multipolar spindles by pole splitting and four-wall confinement restraining multipolar spindles by the inhibition of splitting and the enhancement of clustering. (a) Time-lapse images from NEB to telophase show pole splitting under no confinement. (b) Cell under $5\ \mu\text{m}$ height confinement suffering from twice the splitting followed by tetrapolar division. (c) Among all the multipolar spindles, the fraction of pole splitting, clustering, “splitting-clustering” (first split and then cluster), “clustering-splitting” (first cluster and then split), maintaining (pole number of a multipolar spindle remaining unchanged during the mitosis process), and (d) corresponding duration from NEB to anaphase or death under no confinement ($n = 107$) and two-wall confinement ($n = 98, 111,$ and 104). We use the Mann-Whitney test with $*p < 0.05$, $**p < 0.01$, and $***p < 0.001$. The data of clustering, splitting-clustering, and clustering-splitting have been omitted in panel (d) since the data were too few to be statistically significant. (e) Fraction of cells with one or more pole splittings, and (f) the corresponding duration from NEB to anaphase or death under no confinement ($n = 70$) and two-wall confinement ($n = 85, 87,$ and 61). We use the Mann-Whitney test with $**p < 0.01$. Time-lapse images from the NEB to telophase show the pole splitting (g) and clustering (h) under four-wall confinement. (i) Among all the multipolar spindles, the fraction of pole splitting, clustering, splitting-clustering, clustering-splitting, and maintaining, and (j) the corresponding duration from NEB to anaphase or death under no confinement ($n = 107$) and four-wall confinement ($n = 59, 59,$ and 80). The data of splitting-clustering and clustering-splitting have been omitted in panel (j). In panel (k), time-lapse images show the splitting-clustering process under four-wall confinement. (l) The fraction of cells with one or more pole splittings under no confinement ($n = 70$) and four-wall confinement ($n = 17, 21,$ and 41). (m) Duration from NEB to anaphase or death compared in the three cases. We use the Mann-Whitney test (n.s., not significant) with $p = 0.83393$, $p = 0.57714$. All scale bars are $10\ \mu\text{m}$.

tubulin in fluorescent images rather than centrosomes [32,40]. For cells without any confinement, pole splitting occurs in about 70% of multipolar spindles [Fig. 2(c)]. For two-wall confinement, the fraction increases to 90% as the channel height decreases from 7 to 3 μm [Fig. 2(c)], which is in good agreement with earlier experimental observations [32]. Furthermore, among cells with pole splitting, the fraction of cells pole splitting multiple times (≥ 2) also increases as the channel height decreases [Figs. 2(e) and S5(b)]. Therefore, after pole splitting several times, the frequency of cells with 4, 5, and even more poles is much higher in extreme height confinement [Figs. S3 and S5(a)]. Taken together, these results indicate that two-wall confinement leads to a higher fraction of multipolar spindles by pole splitting.

Strikingly, under four-wall confinement, although cells could still undergo pole splitting [Fig. 2(g) and movie S1 [38]], its fraction in multipolar spindles significantly decreases [Fig. 2(i)]. In particular, the fraction decreases to 29% as the channel width decreases to 8–12 μm . At the same time, the fraction of cells pole splitting multiple times (≥ 2) also decreases with the decrease of channel width [Fig. 2(l)]. Therefore, contrary to the stimulation effect of two-wall confinement, four-wall confinement tends to restrain pole splitting.

Unexpectedly, under four-wall confinement, pole clustering, i.e., the coalescence of two poles into one pole, increases remarkably as the channel width decreases [Figs. 2(h) and 2(i) and movie S1 [38]]. In contrast, there is nearly no pole clustering under two-wall confinement [Fig. 2(c)]. It is worth noticing that a considerable fraction of cells undergo pole splitting and clustering successively, which is termed “split-cluster” [Fig. 2(i)]. For example, Fig. 2(k) and movie S1 [38] show that one pole of a bipolar spindle in the $10 \times 10 \mu\text{m}^2$ channel splits into two poles initially but fails to reach a new equilibrium state, and finally, the two poles cluster together again. This suggests that pole splitting is reversible under four-wall confinement, and the split poles can be rescued by pole clustering through certain mechanisms. On the contrary, pole clustering under no confinement and two-wall confinement is impaired, so pole clustering is very rare, resulting in either multipolar division or death. Taken together, we conclude that two-wall confinement leads to an increased fraction of multipolar spindles by pole splitting, but four-wall confinement restrains multipolarity by the inhibition of pole splitting and the enhancement of pole clustering.

We further investigate how pole splitting and clustering affect the duration of cell division. We find that, compared to no confinement, both two-wall and four-wall confinement lead to longer mitotic delay or even mitotic arrest, measured as the duration from NEB to anaphase or death [Figs. 2(d) and 2(j)]. Moreover, cells subjected to pole splitting or pole clustering take much longer than cells

with a constant number of poles [Figs. 2(d) and 2(j)]. This is consistent with the previous experimental observation that doubling the centrosome number of RPE-1 cells prolongs mitosis, on account of the coalescence of a tetrapolar spindle into a tripolar or bipolar spindle [41]. Finally, we find that cells pole splitting multiple times (≥ 2) would suffer longer mitotic delays [Figs. 2(f) and 2(m)], but the duration from NEB to anaphase or death appears to be independent of the architecture of confinement [Fig. 2(m)].

C. Increase of pole splitting under two-wall confinement, associated with chromosome scattering during the prometaphase and chromosome crowding during the metaphase

To explore the mechanism of pole splitting under two-wall confinement, we first investigate the chromosome distribution at early mitosis. We find that cells are subjected to severe misalignment and scattered distribution of chromosomes under the extreme height confinement (3 and 5 μm), minor misalignment under 7- μm height confinement, and nearly no misalignment under 10- μm height confinement [Fig. 3(a)]. This is confirmed by the polar radius of gyration about the centroid of the projected chromosomes R_c , which becomes larger when the confinement height becomes smaller, indicating that tighter confinement leads to more severe chromosome misalignment and scattering [Figs. 3(b) and 8(d); see details in Appendix A 7]. The scattered distribution of chromosomes correlates with pole splitting (Fig. S6 and movie S2) due to the limited microtubule length [32,40,42,43] and abnormal forces generated by misaligned chromosomes [6]. Moreover, the flattened cells exhibit continuous blebbing [Fig. 3(a)] [32,44,45], which is very large under extreme height confinement. The scattering chromosomes could be carried into the blebs, ultimately leading to the formation of micronuclei (Fig. S7 and movie S2), which further impairs the fidelity of chromosome segregation.

Besides the scattered distribution of chromosomes during the prometaphase, pole splitting is correlated with the crowding of chromosomes due to the limited space during the metaphase. As shown in Fig. 3(f), under 5- μm height confinement, chromosomes initially self-assemble to form a very short and thick metaphase plate within a bipolar spindle. However, after a long mitosis arrest, the short and thick metaphase plate is bent into a long and thin metaphase plate by pole splitting two times, resulting in the tetrapolar division [Figs. 3(f) and S8 and movie S3]. Thus, we conclude that the increase of pole splitting under two-wall confinement [Fig. 2(c)] is associated with the scattered distribution of chromosomes during the prometaphase and the loss of accommodation for the equatorial plate during the metaphase.

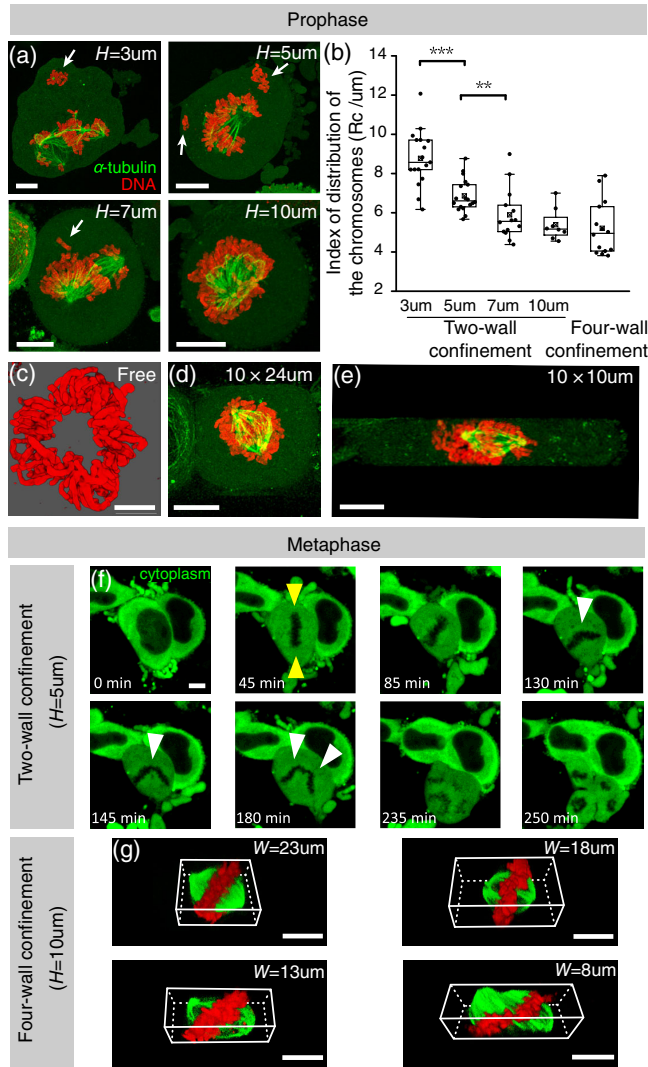


FIG. 3. Increase of pole splitting under two-wall confinement associated with chromosome scattering during the prometaphase and chromosome crowding during the metaphase. (a) Images of scattered chromosome distribution (arrows) during the early prometaphase under two-wall confinement with stained α tubulin (green) and DNA (red). The scale bar is $10\ \mu\text{m}$. (b) Quantification of the degree of chromosome misalignment under two-wall confinement ($n = 17, 18, 14,$ and 8) and four-wall confinement ($n = 24$). We use the Mann-Whitney test with $**p < 0.01$ and $***p < 0.001$. (c) Three-dimensional reconstruction image of toroidal chromosome distribution under no confinement. The scale bar is $5\ \mu\text{m}$. (d, e) Images of chromosome distribution under four-wall confinement. The scale bar is $10\ \mu\text{m}$. (f) Time-lapse images of chromosome arrangement under $5\text{-}\mu\text{m}$ height confinement. The short and thick chromosome plate (yellow arrowhead) bends into a long and thin chromosome plate by pole splitting (white arrowhead), due to the loss of appropriate accommodation for the bipolar chromosome plate. The scale bar is $10\ \mu\text{m}$. (g) Three-dimensional reconstruction images of the chromosome metaphase plate under four-wall confinement. Appropriate four-wall confinement can provide adequate space to accommodate all chromosomes by tilting the metaphase plate during the metaphase. The scale bar is $10\ \mu\text{m}$.

D. Four-wall confinement controlling cell shape, in turn regulating multipolar spindle configuration, and pole splitting and clustering

Under four-wall confinement, we find that when the channel height or width is very small, cells cannot be confined in the channels by using our method, and it is not physiologically realistic in normal epithelial tissue architecture. Thus, here we focus on appropriate four-wall confinement [$H > 8\ \mu\text{m}$ and $W > 8\ \mu\text{m}$ in Fig. 1(d)]. We find that similar to free cells, appropriate four-wall confinement rarely results in scattered distribution of chromosomes during the prometaphase [Figs. 3(c)–3(e)], in agreement with previous observations [46–48]. Appropriate four-wall confinement can provide enough space to accommodate all chromosomes by tilting the metaphase plate during the metaphase [Figs. 3(g) and S9]. However, these observations only partly explain why appropriate four-wall confinement can restrain multipolar spindles [Fig. 2(i)].

To better understand the behaviors of multipolar spindles under four-wall confinement, we modify our previous computational model [42,49,50] by introducing multiple spindle poles into the model and considering pole splitting and clustering [Fig. 4(a) and movie S4]. For simplicity, we consider four spindle poles, among which one pair of poles is clustered together initially, and the initial positions of these poles are randomly distributed inside the cell; thus, both pole splitting and clustering can be studied. Our numerical simulations demonstrate that the fraction of pole splitting increases in round cells, in comparison with elongated cells [Fig. 4(b)]. In contrast, pole clustering is more frequent in elongated cells than in round cells [Fig. 4(b)]. These results further confirm our previous experimental observations [Fig. 2(i)]. Our results are also in good agreement with the experimental observation that round cells exhibit a bias toward multipolar spindles, but an elongated cell shape promotes pole clustering and bipolar spindle mitosis [16].

Interestingly, our simulation also predicts that four-wall confinement can control the cell shape, which in turn effectively regulates the equilibrium configuration of multipolar spindles, which was further verified by our experiment [Figs. 4(c) and 10]. As shown in Figs. 4(c) (top) and 4(e), most tripolar spindles are regular triangles at equilibrium in wide channels since the cell aspect ratio equals 1 in this case. In contrast, a higher fraction of tripolar spindles become obtuse triangles that consist of two smaller bipolar spindles sharing one pole as the aspect ratio increases [Fig. 4(c), middle], and some spindles even become straight lines in extremely narrow channels [Fig. 4(c), bottom]. The regulation of multipolar spindle configurations by cell shape is further confirmed by the shape index of multipolar spindles, S , which equals 1 for a regular triangle and 0 for a straight line [Fig. 4(d); see Appendix A 8]. Moreover, although we find that the

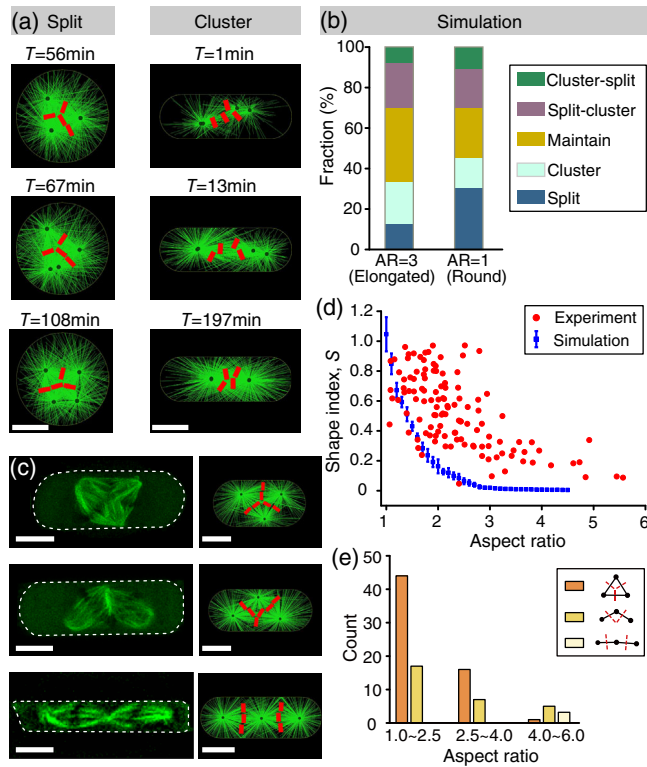


FIG. 4. Four-wall mechanical confinement controlling cell shape, which in turn regulates multipolar spindle configuration, and pole splitting and clustering. (a) Pole splitting and clustering process under four-wall confinement in simulation. The scale bar is 10 μm . (b) Fraction of pole splitting, clustering, splitting-clustering, and clustering-splitting under four-wall confinement in simulation ($n = 200, 200$). AR stands for aspect ratio. (c) Three typical configurations of tripolar spindles in cells with different aspect ratios from the experiment and simulation. The scale bar is 10 μm . (d) Shape index of tripolar spindles as a function of cellular aspect ratio. (e) Quantity of three configurations of tripolar spindles in cells with different aspect ratios in the experiment.

fraction of obtuse triangles and straight lines in all tripolar spindles increases as the channel becomes narrower, the absolute quantities decrease [Fig. 4(e)], which is consistent with our previous observation [Fig. 1(i)].

E. Enhancement of pole clustering and inhibition of pole splitting under four-wall confinement induced by the pole-cortex interaction mediated by cell shape

Although our computational model is comprehensive and robust, it is also complicated. To get more insight into how mechanical confinement regulates the configuration, and pole splitting and clustering in multipolar spindles, we further develop a simplified theory. In fact, previous studies have proposed that spindle pole separation and positioning depend on both pole-pole and pole-cortex interactions, which explains that the spatial distribution of the cortical cues can regulate the spindle configurations on different

micropatterns (H-shaped or Y-shaped) [16]. Some other theoretical works showed that the combination of centrosome-centromere, centrosome-cortex, centrosome-kinetochore, and centrosome-chromosome arm interaction [51], or the torque rotating chromosome arms instead of the interaction between the spindle and cell cortex [52], can promote spindle bipolarity. Moreover, the probabilistic model is used to show that, through natural selection, the tetraploid cell can asymmetrically cluster supernumerary centrosomes into a bipolar configuration, forming a daughter cell with three centrosomes and another daughter cell with a single centrosome, which is favored for long-term survival [53]. However, these models [16,51–53] cannot be used to find the difference between various forms of mechanical confinement that cells encounter in normal tissues and tumor tissues or how they affect multipolarity and chromosome segregation fidelity. Therefore, based on previous studies [16,51,52] and the interacting particle model [51,54], we develop a minimal theoretical model, in which spindle poles and the cortex are considered as particles interacting with each other by pairwise interactions in a distance-dependent manner [Fig. 5(a)], and the movement, positioning, splitting, and clustering of spindle poles are governed by the competition between the pole-pole interaction and the pole-cortex interaction.

In the absence of the influence of the cell cortex, we can obtain the interaction force between two poles as the function of the pole-pole distance from the simulation [Fig. 5(c)], which can be well fitted by Eq. (C2). The integration of the fitted interaction force yields the pairwise pole-pole interaction energy, which is a double-well potential [51,55–57] with two minimums representing two stable states, i.e., the clustered and split states of the two poles [Fig. 5(d)] (see details in Appendix C). This is strongly reminiscent of a reversible chemical reaction, where the splitting reaction and clustering reaction should overcome energy barriers ΔE_{split} and $\Delta E_{\text{cluster}}$, respectively [Fig. 5(d)]. If there are n spindle poles, the total pole-pole energy should be a multiple-well potential with many metastable spindle configurations (Fig. 11). The superposition of the pole-pole interaction and the pole-cortex interaction yields the total energy of the system with shifted equilibrium spindle configurations and altered energy barriers ΔE_{split} and $\Delta E_{\text{cluster}}$ (see Appendix C for more details).

The pole-cortex interaction, including the contributions from the pushing or pulling force generated by microtubule polymerization and various molecular motors [58–62], is given by an integral on the whole cortex (see Appendix C for details). Qualitatively, the pole-cortex interaction becomes more repulsive when the pole approaches the cortex, and it diminishes when the pole retreats from the cortex [Fig. 5(b)].

Based on experimental data within channels with various widths, we calculate how the total energy of the system

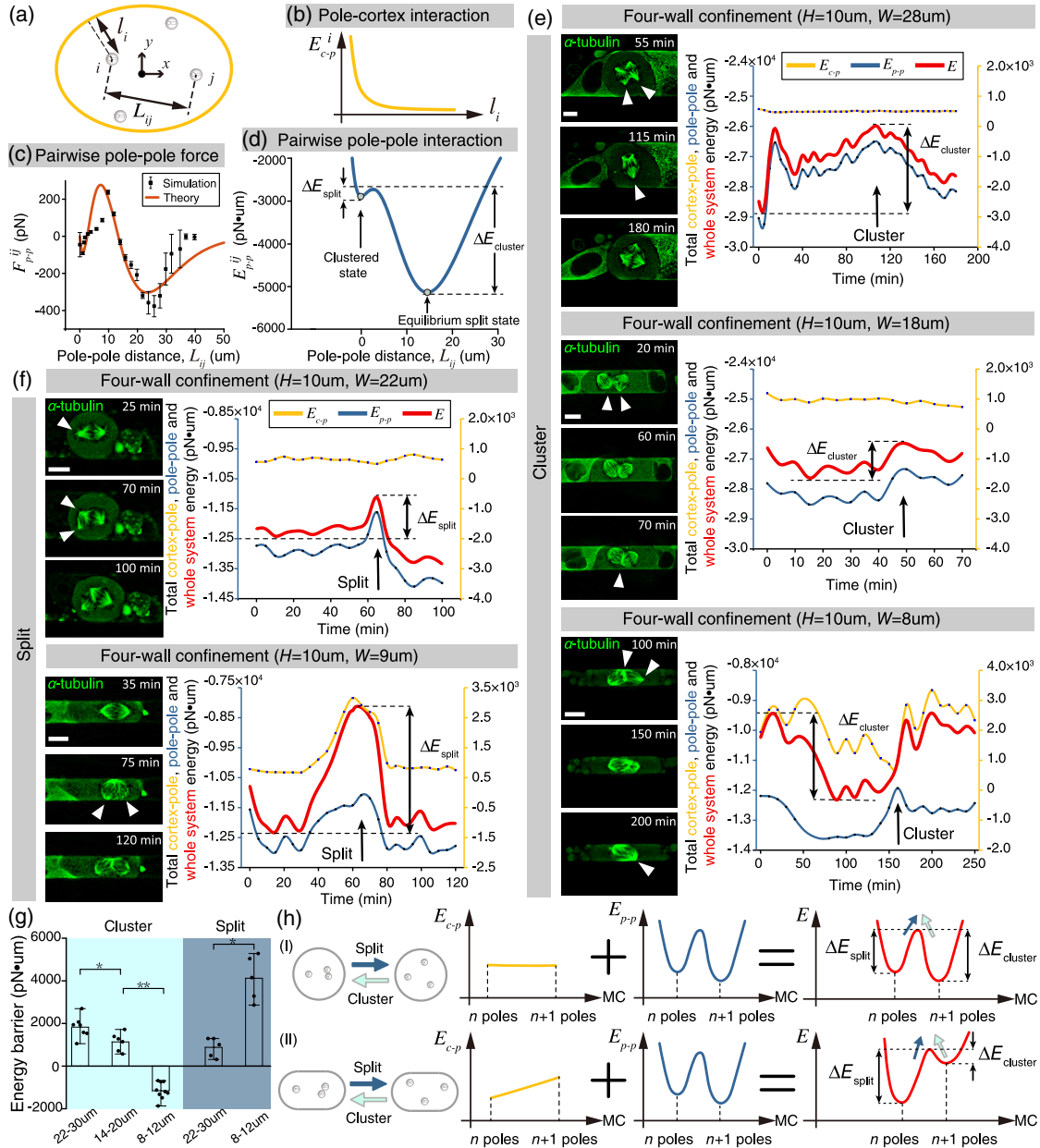


FIG. 5. Enhancement of pole clustering and inhibition of pole splitting under four-wall confinement induced by the pole-cortex interaction mediated by cell shape. (a) Schematic of the theoretical model. (b) Pole-cortex interaction between the i th pole and the cortex, E_{c-p}^i , becoming more repulsive when the pole approaches the cortex and rapidly diminishing when the pole moves far away from the cortex. Note that l_i is the minimum distance between the i th pole and the cortex. Here, $E_{c-p} = \sum_{i=1}^n E_{c-p}^i$ denotes the total pole-cortex interaction. (c) Pairwise pole-pole interaction force between the i th and the j th poles, F_{p-p}^{ij} , as a function of pole-pole distance L_{ij} , calculated in our simulation and fitted by the theoretical model. (d) Pairwise pole-pole interaction energy between the i th and the j th poles, E_{p-p}^{ij} , which is a double-well potential with two stable states, i.e., the clustered and split states. Total pole-pole energy landscape of multiple poles, i.e., $E_{p-p} = \sum_{i,j=1}^n E_{p-p}^{ij}$. (e-f) Calculated time evolution of the pole-pole interaction energy (E_{p-p}), pole-cortex interaction energy (E_{c-p}), and whole energy of the system ($E = E_{p-p} + E_{c-p}$) during pole clustering and splitting in microchannels with different widths based on the experimental data. The scale bar is $10 \mu\text{m}$. (g) Energy barrier of pole clustering ($\Delta E_{\text{cluster}}$) and splitting (ΔE_{split}) obtained from experiments ($n = 7, 6, 9, 5, 5$). We use the Mann-Whitney test with $*p < 0.05$ and $**p < 0.01$. (h) Mechanical confinement influencing the energy barriers of pole clustering and splitting. In wide channels, all spindle poles are far away from the cell boundary, and the pole-cortex interaction is negligible compared to the pole-pole interaction. In narrow channels, the average distance between poles and the cell cortex is smaller, and the contribution of the pole-cortex interaction becomes significant. Thus, the four-wall mechanical confinement changes the energy landscape of the system by increasing ΔE_{split} and decreasing $\Delta E_{\text{cluster}}$, indicating that it is easier for pole clustering but more difficult for pole splitting in narrower channels. MC stands for multipolar configuration.

evolves with time [Figs. 5(e)–5(g)]. We find that the energy barrier for pole clustering ($\Delta E_{\text{cluster}}$) is quite large within a 22–30- μm -wide channel [Figs. 5(e) and 5(g) and movie S5] but relatively small in a 14–20- μm -wide channel [Figs. 5(e) and 5(g) and movie S6]. In an 8–12- μm -wide channel, $\Delta E_{\text{cluster}}$ even becomes negative [Figs. 5(e) and 5(g) and movie S7], which indicates that the energy barrier vanishes in extremely narrow channels. In contrast, the energy barrier for pole splitting (ΔE_{split}) increases as the channel width decreases from 22–30 μm to 8–12 μm [Figs. 5(f) and 5(g) and movies S8 and S9].

These results could be easily understood in the following simple physical picture [Fig. 5(h)]. In wide channels, the aspect ratio is small, and the cell nearly remains circular; thus, all spindle poles are far away from the cell boundary. Thus, the change of the pole-cortex interaction is very small when pole splitting or clustering happens, so the total energy is mainly determined by the pole-pole interaction [Fig. 5(h)(I)]. In narrow channels, the aspect ratio is large, and the cell is elongated due to the confinement; thus, the average distance between poles and the cortex is smaller, and the contribution of the pole-cortex interaction becomes significant [Fig. 5(h)(II)]. In this case, the four-wall mechanical confinement changes the energy landscape of the system by increasing ΔE_{split} and decreasing $\Delta E_{\text{cluster}}$ [Fig. 5(h)(II)], indicating that it is easier for pole clustering but more difficult for pole splitting to occur in narrower channels. The pole splitting becomes less and less favorable as the aspect ratio of cells increases. In the limit case, the double-well potential will transit to a single-well potential so that $\Delta E_{\text{cluster}}$ vanishes [Fig. 5(e) and movie S7]. Therefore, we conclude that the enhancement of pole clustering and the inhibition of pole splitting under four-wall confinement are induced by the pole-cortex interaction mediated by cell shape.

F. Disrupting the astral microtubules to confirm the pole-cortex interaction can enhance pole clustering and inhibit pole splitting under four-wall confinement

To further justify the mechanism we proposed above, we disrupt the pole-cortex interaction by low dose nocodazole treatment (20 nM) [Fig. 6(a)], which has been shown to selectively depolymerize astral microtubules [21,61,63,64] but has no effect on the assembly of bipolar and multipolar spindles [65] [Figs. 6(b) and 6(c)]. In comparison with control cells (DMSO), nocodazole treatment results in more multipolar spindles in 8–12 μm channels but no significant changes in wider channels [Fig. 6(d)]. Cells treated with nocodazole suffered more pole splitting than control cells, especially in 8–12 μm channels where the fraction of pole splitting increased from 33% to 51% [Fig. 6(e)]. Furthermore, the fraction of pole splitting multiple times (≥ 2) also increased after nocodazole treatment especially in narrow channels [Fig. 6(f)]. Remarkably, the fraction of pole splitting after nocodazole treatment was

almost the same in all the channels [Figs. 6(e) and 6(f)]; i.e., the fraction of pole splitting was not sensitive to the channel width anymore, which further confirmed that the cell shape can effectively regulate the pole splitting through the pole-cortex interaction. The fraction of pole clustering decreased slightly after nocodazole treatment [Fig. 6(e)]. In particular, nocodazole-treated cells exhibit a deficient ability of pole clustering from tetrapolar spindles to bipolar spindles [Fig. 6(g)]. It is worth noticing that the effect of disrupting the pole-cortex interaction in narrow channels is more remarkable than that in wider channels [Figs. 6(e)–6(g)], which again confirms our theoretical prediction that the contribution of the pole-cortex interaction becomes more significant in narrow channels due to the elongated cell shape.

Furthermore, previous research has suggested that myosin-dependent cortical contraction acting on astral microtubules plays an important role in spindle assembly [16,66]. Along this line, the inhibition of cell contractility and cortical tension could strongly affect the actin cortex, which in turn suppresses the interaction of the cell cortex and astral microtubules [16,66], i.e., pole-cortex interaction. To test this idea, we treat the cells with ROCK inhibitor Y27632 or myosin II ATPase inhibitor blebbistatin to inhibit myosin-dependent cortical contraction. The results show that the suppression of the pole-cortex interaction by inhibiting cortical contraction leads to more pole splitting and less pole clustering, in comparison with the control group [Figs. 6(e)–6(g)]. Taken together, these results further demonstrate that the enhancement of pole clustering and inhibition of pole splitting under four-wall confinement are induced by the pole-cortex interaction mediated by cell shape.

III. DISCUSSION

In this work, we utilized microchannels to mimic various degrees of mechanical confinement from a complicated epithelial tissue environment, and we explored how various forms of mechanical confinement regulate the behaviors of multipolar spindles (Fig. 1). We found that two-wall confinement leads to an increased fraction of multipolar spindles by pole splitting, while four-wall confinement restrains multipolarity by the enhancement of pole clustering and the inhibition of pole splitting. We further demonstrated that the four-wall confinement changes the cell shape, which influences the interaction between the cell cortex and spindle poles and thus changes the energy barriers of pole splitting and pole clustering. These results might be easily understood in the following simple physical picture. Under four-wall confinement, there are only two opposite directions, along the cell's long axis, where the poles can go, so they are effectively pushed together to form bipolar spindles. In contrast, the two-wall confinement only limits cell height (the z direction), but the other

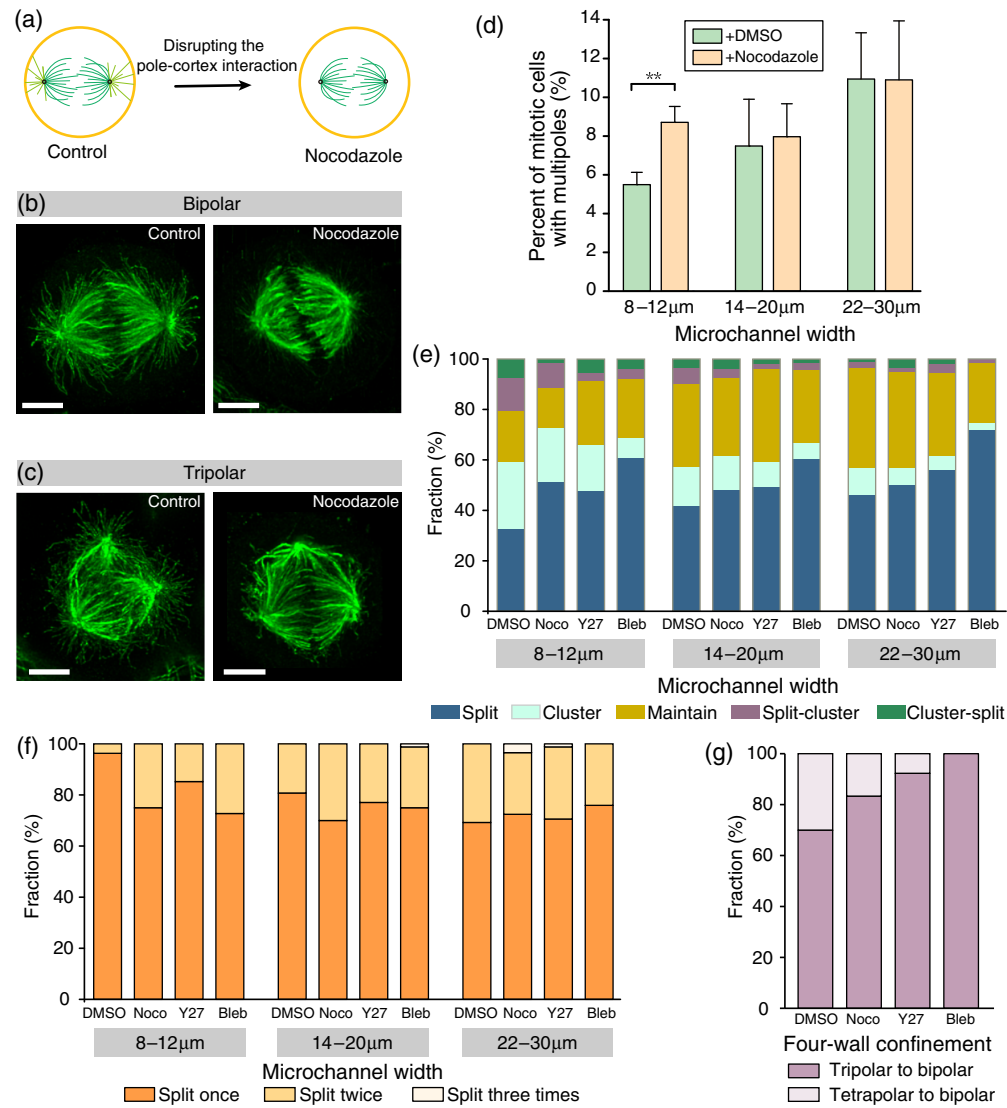


FIG. 6. Disrupting the astral microtubules and confirming the pole-cortex interaction can enhance pole clustering and inhibit pole splitting under four-wall confinement. (a) Schematic diagram showing the disruption of the pole-cortex interaction by low-dose nocodazole treatment (20 nM). (b,c) Bipolar and tripolar spindles in 20-nM nocodazole-treated cells showing the selective disruption of astral microtubules. The scale bar is 5 μm . (d) Percentage of multipolar spindles in control (DMSO) and nocodazole-treated (Noco) cells under four-wall confinement ($n = 374, 574, 524, 850, 502, 541$). We use a two-sample t-test with $**p < 0.01$. (e) Among all the multipolar spindles, the fraction of pole splitting, clustering, splitting-clustering, clustering-splitting, and maintaining in cells treated with DMSO, 20-nM Noco, 10- μm ROCK inhibitor Y27632 (Y27), and 10- μm myosin II ATPase inhibitor blebbistatin (Bleb) under four-wall confinement [$n = (83, 70, 148, 51)$; (122, 83, 348, 139); (84, 58, 151, 75)]. (f) The fraction of cells with one or more pole splittings in DMSO and Noco/Y27/Bleb-treated cells under four-wall confinement [$n = (27, 36, 61, 33)$; (52, 40, 170, 84); (39, 29, 85, 54)]. (g) Comparison of pole clustering from tripolar or tetrapolar spindle to bipolar spindle in DMSO and Noco/Y27/Bleb-treated cells under four-wall confinement ($n = 30, 12, 39, 10$).

two directions in the xy plane are free. The height confinement leads to a strong pole-cortex interaction in the z direction, which can only confine all the poles in the xy plane. But the contribution of the pole-cortex in the xy plane is almost negligible, so there is no additional driving force for pole clustering in this case. Moreover, the strong confinement in the cell height will further lead to the scattered distribution of chromosomes during the

prometaphase and the loss of accommodation for the equatorial plate during the metaphase, resulting in an increase of the pole splitting under two-wall confinement. Because of these two factors, the multipolar spindle is more frequent under two-wall confinement.

Currently, researchers generally regard the spatial confinement as a challenge for various cell behaviors. For example, uncontrolled proliferation of cancer cells *in vivo*

generates compressive stress within tumors, and the stress accumulated during tumor growth makes cancer cells densely packed [29,30] and even collapses blood and lymphatic vessels within the tumor [31]. Furthermore, the overcrowded environment, e.g., severe height confinement, can result in the fragmentation and splitting of the spindle pole so that the probability of multipolar spindles and multidaughter cell division remarkably increases [32–34]. The lack of space in crowded environments also presents cells with a significant challenge for cell migration so that cells have to adopt various migration modes [24,26,27,36] to squeeze through narrow pores or channels. In contrast, our results show that appropriate spatial confinement similar to normal tissue architecture can suppress multipolar mitosis and ensure chromosome segregation fidelity. Therefore, the spatial confinement can be a protection instead of a challenge for cells in this case.

The contradictory results under two-wall and four-wall confinements address the sensitivity of cell behaviors to mechanical constraints from extracellular microenvironments [67,68]. The changes of the form and degree of mechanical constraints within tissue architecture may lead to opposite influences on cellular behaviors. For example, Rous-sarcoma-virus-infected embryos develop normally without oncogenesis, whereas once the cells are removed from the embryo and placed in culture, they express the transformed phenotype [69,70]. Furthermore, primary epithelial cells and hepatocytes present faithful chromosome segregation within native tissue architecture or organoid culture, but missegregate chromosomes when dissociated from tissues [5,7,8,28].

Since the microenvironment becomes overcrowded in tumors, our findings may explain why the multipolar spindle is very rare in normal tissues but much more prevalent in many tumors. Actually, every cell in our body communicates with extracellular surroundings, and an appropriate microenvironment acts as a suppression to tumorigenesis as long as the normal tissue homeostasis is essentially controlled [67]. On the other hand, once the appropriate extracellular microenvironment is disrupted, it may become a promotion of cancer progression [67]. For example, increased mammary tissue density may exist long before breast cancer occurs [71–73]. Thus, the changes of the extracellular microenvironment, i.e., either the loss or enhancement of mechanical confinement, possibly triggers multipolarity and promotes cancer progression [2,67]. This also suggests that the administration of drugs or chemotherapeutics for modifying the tumor microenvironment could be a potential cancer therapy [67]. In fact, there are many trials relevant to microenvironmental therapies, and some of these therapies have already been approved by the US Food and Drug Administration (FDA) for several cancer treatments [67]. For instance, bevacizumab (Avastin) is a FDA-approved treatment for metastatic colorectal cancer that inhibits the signaling between the

tumor and endothelial cells in the microenvironment [74]. Thus, a better understanding of the mechanism of an extracellular microenvironment regulating cellular behaviors could have a profound impact on cancer diagnosis and clinical trials targeting the tumor microenvironment [67,68].

In this work, note that we only consider how the mechanical confinement from the extracellular microenvironment changes the cell shape and in turn affects the pole-cortex interaction. However, the extracellular microenvironment usually contains other cells as well [67,75,76], which causes cells to be exposed to a complex network of signals in their environment [75]. Thus, cells can dynamically communicate with their extracellular microenvironment through cell-substrate adhesion and cell-cell adhesion, as well as hormones and other soluble factors, which could be converted to the intracellular signals that regulate cell behaviors [67,75]. Although some genes for cell-substrate and cell-cell adhesion that are required to suppress multipolar divisions have been identified [16], how these factors influence the assembly of multipolar spindles still needs further investigation.

ACKNOWLEDGMENTS

This work was partially carried out at the University of Science and Technology of China Center for Micro and Nanoscale Research and Fabrication, and we especially thank Liu Wen, Wang Xiu-xia, and Peng Fang-fang for their technical assistance. This work was supported by the National Natural Science Foundation of China (Grants No. 12025207 and No. 11872357), and the Fundamental Research Funds for the Central Universities.

APPENDIX A: MATERIALS AND METHODS

1. Cell culture and stable cell lines

HeLa cells and MDA-MB-231 cells were cultured in DMEM (Gibco; Life Technologies) supplemented with 10% FBS (Gibco; Life Technologies) and 1% penicillin-streptomycin (Gibco; Life Technologies) at 37 °C and 5% CO₂ in humid conditions. Stable cell lines expressing GFP- α tubulin were transfected with lentivirus. Cells were selected by 5- μ g/mL puromycin (InvivoGen) and sorted by fluorescence activated cell sorting (FACS).

2. Microchannel fabrication

The microchannels for shaping cells were made from polydimethylsiloxane (PDMS) by means of a photolithographic protocol [35–37] [Fig. 1(b)]. Briefly, the photoresist (AZ6112 or AZ5214) was spin coated onto a 4-inch silicon wafer. The wafer was baked on a hot plate for 90 seconds at 100 °C and then exposed to 12.6 mW/cm² UV light (optical aligner MA/BA6, SUSS, Garching bei Munchen, Germany) for 2.2 seconds. After that, the wafer was etched by inductively coupled plasma (PlasmaPro System100 ICP380; Oxford Instruments, Abingdon,

United Kingdom). PDMS (Sylgard 184, Dow Corning) at a ratio of 10:1 was poured onto the master and peeled off from the master after baking at 65 °C for 12 hours. Finally, the PDMS was cut into 10 × 10-mm pieces that fit on a standard 35-mm glass-bottom dish (NEST,801001).

Just before use, the PDMS piece was treated with plasma cleaner (PDC-002, Harrick, Stockton, CA) in O₂ for 1 minute to make it hydrophilic. A 50-μL drop of cells in culture medium was then placed onto the center of the glass-bottom dish (NEST,801001) and allowed to settle onto the dish for about 2 minutes. The PDMS piece was then placed on top of the liquid drop, and the culture medium was gently sucked from the periphery of the PDMS piece to the microchannels, which slowly pushed the cells into the microchannels. To confine the cells into the microchannels tightly, a glass block of size 10 × 10 × 20 mm is placed on top of the PDMS. A sufficient medium was gently added to the culture dish to keep cells alive for at least 48 hours.

3. Drug treatment and live imaging

For cell-cycle synchronization, cells were first blocked in G1/S with 2.5-mM thymidine (T1895, Sigma) for 16 hours and then released in fresh culture medium for 10 hours to enrich mitotic cells. For experiments with no confinement, cells were synchronized with thymidine for 16 hours and washed with PBS. After the release to fresh culture medium for 10 hours, the frequency of multipolar spindles was calculated, and the evolution of the mitotic cells was imaged. For two-wall or four-wall confinement experiments, cells stably expressing GFP- α tubulin were synchronized with thymidine at a final concentration of 2.5 mM for 16 hours, followed by washing with PBS three times for 5 minutes each; cells were then seeded into the microchannels as described above. After 10 hours of the culture being in the microchannels, the number of mitotic cells with bipolar and multipolar spindles was counted, and the behavior of the mitotic cells was imaged using a time-lapse fluorescence microscope within 48 hours.

Nocodazole (M1404, Sigma) was used at 20 nM, and ROCK inhibitor Y27632 (Y27) and myosin II ATPase inhibitor blebbistatin (Bleb) were used at 10 μM. Equivalent volume dimethyl sulfoxide (DMSO, Sigma) treatment was used as control. The final concentration of DMSO in all experiments was less than 0.1%.

For live cell imaging, cells were imaged with a Leica DMi8 fluorescence microscope with a 20 × lens (numerical aperture, NA 0.75 or NA 0.8) equipped with temperature and CO₂ controlling environmental chambers (WSKM, TOKAI HIT), and images were acquired every 5 minutes. For experiments with no confinement, multi-dimensional images with z-stacks of 1 μm per step covering the entire volume of the cells were acquired every 5 minutes.

4. Immunofluorescence

For immunofluorescence, cells were washed with PBS and fixed with 4% paraformaldehyde (PFA) (Sigma) in PBS at room temperature for 10 minutes. Fixed cells were washed with PBS for 5 minutes, permeabilized with 0.1% Triton X-100 (Sigma) in PBS (0.1% PBST) for 10 minutes, and blocked with 4% BSA in 0.1% PBST for 20 minutes. Primary antibodies [α tubulin (ab6160; 1:1000, Abcam) or α Tubulin-FITC (F2168; 1:1000, Sigma), γ tubulin (T5362; 1:500, Sigma)] were diluted in blocking solution (4% BSA in 0.1% PBST) and incubated overnight at 4°C. Cells were washed three times with 0.1% PBST for 5 minutes each time. Secondary antibodies [Alexa Fluor 488 (rat; 1:1000, Abcam), Alexa Fluor 568 (mouse; 1:1000, Sigma)] were diluted in blocking solution with 5 μg/mL Hoechst 33342 dye (Sigma) and incubated in the dark for 1 hour at room temperature. Cells were washed twice with 0.1% PBST for 5 minutes, followed by a PBS wash for 5 minutes.

5. Image processing and analysis

Displayed images were processed using Leica Application Suite X (LAS X), a software platform for all Leica microscopes from Leica Microsystems, or Image J, where contrast or brightness was changed across the field, and deconvolution was applied by Huygens Essential when necessary. For images of multidimensional z-stacks, projection or extended depth of field was processed by LAS X.

6. Details of phase diagram

Based on the average cell volume of HeLa cells [Fig. 1(c) in the main text], we propose a phase diagram to distinguish the level of mechanical confinement during mitosis [Fig. 1(d) in the main text]. We assume the width and height of microchannels are W and H , respectively. The phase diagram contains three regions, i.e., no confinement (cell rounding freely during mitosis), two-wall confinement (only cell height or cell width is confined during mitosis), and four-wall confinement (both cell height and width are confined). The diagram displays the reflection symmetry about the line $H = W$ due to the intrinsic symmetry of the height and width of microchannels.

Here, we only discuss the case of $H \leq W$, and the result of $H > W$ can be deduced by the exchange of H and W . If we assume the average cell volume of HeLa cells is V and the radius of cells in suspension is R_0 , then we should have $V = 4\pi R_0^3/3$. If both the width and height of microchannels are bigger than R_0 , the cell is not constrained. If $H < 2R_0$, the cell is under two-wall confinement as shown in Fig. 7. In this case, the cell height h is equal to the microchannel height H , while the cell width w is less than the microchannel width W , i.e., $w \leq W$, since the cell width is not constrained. If we assume the lateral surface of the cell is a spherical surface with radius R (Fig. 7), the cell

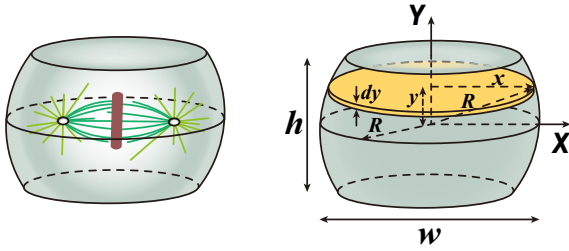


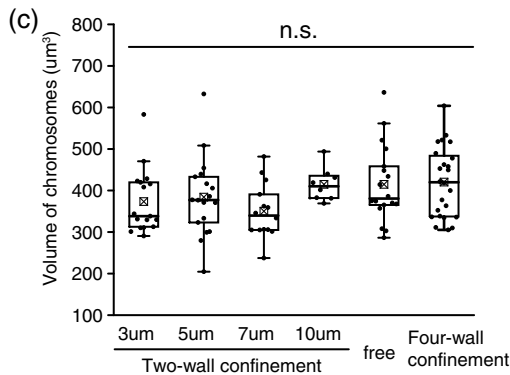
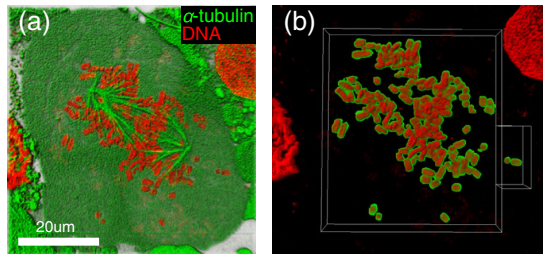
FIG. 7. Schematic for the cell under the two-wall confinement.

width should be the diameter of the equatorial plane, i.e., $w = 2R$. Thus, the cell volume is given by $V = 2 \int_0^{H/2} \pi x^2 dy = 2 \int_0^{H/2} \pi (R^2 - y^2) dy = (\pi/4)w^2H - (\pi/12)H^3$. When $w = W$, the cell volume becomes $V = (\pi/4)W^2H - (\pi/12)H^3$, which yields the boundary between two-wall confinement and four-wall confinement in Fig. 1(c) of the main text.

7. Quantification of the degree of chromosome misalignment

To quantify the degree of chromosome misalignment under two-wall confinement (Fig. 8), we use the radius of gyration of the projected chromosome area R_c to define the index of chromosome distribution as

$$R_c = \sqrt{I_\rho / A}, \quad (\text{A1})$$



where $I_\rho = \int_A \rho^2 dA = \int_A (x^2 + y^2) dA$ is the polar moment of inertia, A is the projected area of chromosomes, and x and y are coordinates with the origin at the center of mass of chromosomes.

We find that R_c becomes larger when the confinement height becomes smaller, indicating that tighter confinement leads to severer chromosome misalignment and scattering [Figs. 3(b) and 8(d)].

It should be noted that even without the scattering of chromosomes, R_c can still increase when cell height decreases since we found that the chromosome volume is conserved under various level of confinements [Fig. 8(c)]. To eliminate this influence on R_c , we calculate the radius of gyration R_d of a solid disk that shares the same volume V and height H with the scattered chromosomes as

$$R_d = \sqrt{\frac{V}{2\pi H}}. \quad (\text{A2})$$

We find that the difference between R_c and R_d still increases as the height of two-wall confinement decreases [Fig. 8(d)], indicating that two-wall confinement indeed results in the scattered distribution of chromosomes.

8. Quantification of the pattern of multipolar spindles

To quantify the configuration of multipolar spindles, we define a shape index as

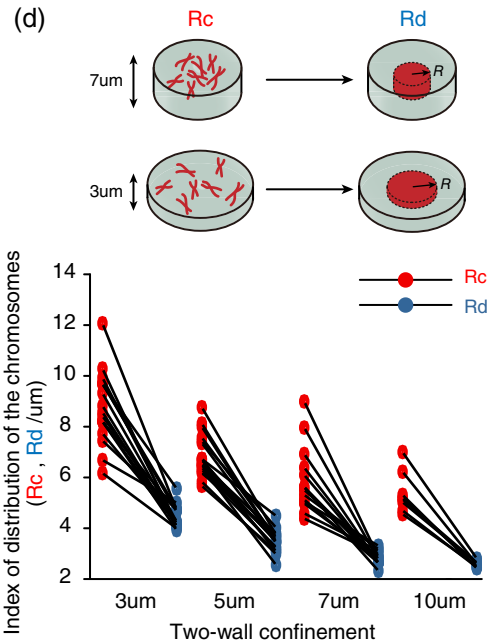
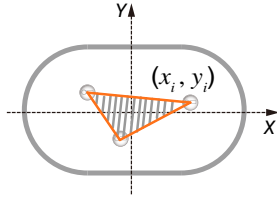


FIG. 8. Two-wall confinement resulting in scattered distribution of chromosomes. (a,b) Discernment of chromosomes by Image J. (c) Chromosome volume under two-wall confinement ($n = 17, 18, 14, 8$), no confinement ($n = 18$), and four-wall confinement ($n = 24$). We use Mood's median test; n.s., not significant; $p = 0.13167$. (d) Difference between R_c and R_d still increasing as the height of two-wall confinement decreases ($n = 17, 18, 14, 8$).

FIG. 9. Definition of the shape indices S .

$$S = \frac{\sum_{i=1}^n y_i^2}{\sum_{i=1}^n x_i^2}, \quad (\text{A3})$$

where x_i and y_i are the coordinates of the i th pole when the cell center is zero and the long axis is the x axis (Fig. 9). Obviously, $S = 1$ represents the regular polygon, and $S = 0$ indicates that all the poles are in a straight line.

APPENDIX B: SIMULATION

To better understand the behaviors of multipolar spindles under four-wall confinement, we perform numerical simulations based on our previous computational model [42,49,50] by introducing multiple spindle poles into the model and considering pole splitting and clustering. In brief, the model takes account of both pushing forces and pulling forces on spindle poles through the interactions of microtubules with the cell cortex, chromosomes, antiparallel microtubules, and cytoplasm. Multiple poles and chromosomes can self-assemble to form the multipolar spindle under these complicated interactions.

1. Nucleation and dynamic instability of microtubules

In the assembly process of mitotic spindles, microtubules can be nucleated at centrosomes, chromosomes [77], or existing microtubules as branches [78]. Since all microtubules interact directly or indirectly with the spindle poles [50,79–81], they are assumed to be nucleated from spindle poles with a nucleation rate of k_0 , and the density of the nucleation rate is uniform $k_0/(2\pi)$ in every direction [42,50]. Additionally, we assume a higher nucleation rate in the direction from spindle poles to chromosomes, where the density of the nucleation rate is $k_n k_0/(2\pi)$ (k_n is a constant larger than 1) [50].

Dynamic instability of microtubules, i.e., the transition between a slowly growing state and a fast shrinking state, is crucial for searching the kinetochore [82]. Here, we make an assumption that the microtubules grow at a speed of v_1 and shrink at a speed of v_2 , and the rescue rate (from a shrinking to a growing state) and catastrophe rate (from a growing to a shrinking state) are defined as k_1 and k_2 , respectively [50]. Therefore, microtubule lengths vary over time, and the dynamics of microtubules are determined by these four constant parameters [50].

2. Bundling of microtubules

Besides their nucleation and dynamics, the bundling of microtubules is crucial for cellular functions, such as kinetochore-microtubule interactions [83]. It has been reported that microtubules are guided to grow along existing microtubules by the minus-end-directed motor kinesin-14 and plus-end tracker EB1 [83], leading to the formation of a microtubule bundle [50]. Microtubule bundles sustain a stronger force to ensure a stable spindle configuration. In our model, an extra nucleation rate, $k_l k_0$, is defined along the direction of the existing kinetochore microtubules [50]. Here, $k_l \ll 1$, and thus it has a negligible influence on the total nucleation rate. Therefore, the microtubules in the kinetochore fibers can be supplied enough due to the extra nucleation and ensure the tension on the sister kinetochores.

Hence, the total nucleation rate of a spindle pole is $k_0^* = k_0 + k_n k_0 \theta / (2\pi) + N k_l k_0$. Here, θ is the total angle range in which chromosomes are reached by growing microtubules, and N is the number of kinetochores connected with this spindle pole by microtubules. Polar microtubules exhibit a higher density than astral microtubules, and the peaks appear at the kinetochores because of the formation of microtubule bundling.

3. Interactions between microtubules and cell cortex

When a growing microtubule encounters the cortex, its polymerization will be blocked so that a pushing force is applied to the cortex [80,84–86], which equals the stall force of microtubules, f_{stall} [42,50]. On the other hand, microtubules can be easily buckled by the pushing force [80,87,88]. According to the Euler buckling formula, the critical force is given by $f = \pi^2 \kappa / l^2$, where κ denotes the bending rigidity and l denotes the microtubule length [42,43,50,58,80,89]. The pushing force equals the critical buckling force after microtubules are buckled [42,43,50,58,80,89]. Taken together, the pushing force generated by the cell cortex f^+ can be given by [42,50]

$$f^+ = \min(f_{\text{stall}}, \pi^2 \kappa / l^2). \quad (\text{B1})$$

Furthermore, we assume that microtubules have a higher catastrophe rate k_2^* [50,58,90], when a pushing force is applied to the microtubule.

In addition to the pushing force, microtubules can also bear a pulling force generated by the cortical dynein [85,91]. In our model, the cortical dyneins bind to microtubules at a rate of k_b^- , which is proportional to the density of unbound motors [50]. We assume uniform density of cortical dyneins; thus, k_b^- is a constant on the cortex [50]. Dyneins walk to the minus-end direction of the microtubule and thus generate a pulling force on the microtubule [85,89,92–94]. The pulling force f^- is velocity dependent [42,43,50,95,96] as

$$f^- = f_0^- \left(1 - \frac{v^-}{v_0^-}\right), \quad (\text{B2})$$

where f_0^- , v_0^- , and v^- are the stall force, the unloaded velocity, and the walking velocity of dynein, respectively.

The dyneins bound to microtubules can unbind, and the unbinding rate k_u^- is load dependent [42,43,97],

$$k_u^- = k_0^- e^{f^-/f_u^-}, \quad (\text{B3})$$

where f_u^- is a characteristic force and k_0^- is the unbinding rate of dynein under a zero load. Microtubules become depolymerization states after dyneins unbind from microtubules [89].

4. Interactions between microtubules and chromosomes

During the assembly of mitotic spindles, only a small fraction of microtubules are blocked by chromosomes because the diameters of the chromosome arms are quite small (around 1 μm) [98]. Moreover, microtubules that are blocked by or close to chromosomes can be captured by the chromokinesin on the chromosome arms [97,99] and the kinetochore. Therefore, in our 2D model, we assume that none of microtubules can be blocked by chromosomes, but the microtubules across the chromosome can be bound by the chromokinesin and kinetochore at rates of $k_{b,c}$ and $k_{b,k}$, respectively [50].

Similar to the pulling force generated by dyneins, the pushing force (f_c^+) generated by the chromokinesin on microtubules is also velocity dependent [97] as $f_c^+ = f_0^+ (1 - v^+/v_0^+)$, where f_0^+ is the stall force of kinesin, v_0^+ is the unloaded velocity of kinesin, and v^+ is the walking velocity of the motor [50]. Similarly, the microtubules can also be buckled when the pushing force generated by the chromokinesin is larger than the Euler buckling force. Taken together, the pushing force generated by chromokinesin f_c^+ is given as [50]

$$f_c^+ = \min \left[f_0^+ \left(1 - \frac{v^+}{v_0^+}\right), \pi^2 \kappa / L^2 \right]. \quad (\text{B4})$$

Here, L is the length between the spindle pole and the binding site, rather than the total length of the microtubule l .

The chromokinesin bound to microtubules can unbind at a rate of $k_{u,c}^+$, which is load dependent [97],

$$k_{u,c}^+ = k_0^+ e^{f_c^+/f_u^+}, \quad (\text{B5})$$

where f_u^+ is a characteristic force and k_0^+ is the unbinding rate of kinesin without a load.

The pulling force is generated on microtubules due to the depolymerization when microtubules are attached to the kinetochore [100]. In our model, the kinetochore region is defined as the central region of the chromosome (about

20% of the chromosome length) [50]. This pulling force is both microtubule-length dependent [101] and velocity dependent [85]. Therefore, the pulling force generated by kinetochore f_k^- is given by [50]

$$f_k^- = l \cdot f_{k,0} \cdot \left(1 - \frac{v^-}{v_0^-}\right), \quad (\text{B6})$$

where l is the microtubule length, $f_{k,0}$ is the force per unit length of the microtubule, and v^- equals the component of the relative velocity between the spindle pole and the chromosome in the microtubule direction. Similarly, the kinetochore bound to microtubules can also unbind at a rate of $k_{u,k}^-$, which is load dependent [42,43,97], as

$$k_{u,k}^- = k_{0,k}^- \cdot e^{f_k^-/f_u^-}, \quad (\text{B7})$$

where $k_{0,k}^-$ is the unloaded unbinding rate of kinetochore.

5. Interactions of microtubules with cytoplasmic motors

Some motors walking along the microtubules and carrying cargo in the cytoplasm can also generate pulling forces and play an important role in the positioning and orientating of mitotic spindles [49,81,102]. Given that the walking velocity of the cytoplasmic motor carrying cargo almost equals the unloaded velocity [103,104], the pulling force induced by a single motor is quite small [Eq. (B2)]. However, the number of binding motors is large; therefore, this cytoplasmic pulling force is considered as microtubule-length dependent because more motors can be bound to a longer microtubule [50,102]. Taken together, the pulling force generated by the cytoplasmic motors on a microtubule is assumed as [42,49,50]

$$f_d^- = \eta l, \quad (\text{B8})$$

where η is the pulling force per unit microtubule length, and l is the total microtubule length.

6. Interactions between antiparallel microtubules

Some molecular motors (e.g., kinesin-5, Ncd, and dynein) can serve as cross-linkers to connect antiparallel microtubules and generate forces on them [17,32,42]. In our model, we take account of both dynein and kinesin, which generate the pulling force and the pushing force, respectively. The two crossing microtubules from different spindle poles can be bound by dynein or kinesin at the rates of $k_{b,r}^-$ and $k_{b,r}^+$ [50]. The forces generated by cross-linker motors are also velocity dependent as in Eq. (B2). Therefore, the velocity of the motor bound on the microtubule needs to be solved first. Generally, we consider the interaction between the p th microtubule from the i th spindle pole and the q th microtubule from the j th pole. Let \mathbf{r}_p and \mathbf{r}_q be the unit vectors along the growing

direction of the microtubules, and \mathbf{r}_p^* and \mathbf{r}_q^* be the unit normal vectors of \mathbf{r}_p and \mathbf{r}_q (rotating 90 degrees counter-clockwise from the microtubule growing direction). The absolute velocity of the motor is [50]

$$\mathbf{V}_i + \phi_p L_p \mathbf{r}_p^* + v_p \mathbf{r}_p = \mathbf{V}_j + \phi_q L_q \mathbf{r}_q^* + v_q \mathbf{r}_q. \quad (\text{B9})$$

Here, the left and the right of the equal sign are the absolute velocities of the motor on the p th and q th microtubules, respectively. The first two items denote the transport velocities of the motor; \mathbf{V}_i and \mathbf{V}_j are the velocity vectors of the i th and j th spindle poles; ϕ_p and ϕ_q are the angular velocities of the microtubules; and L_p and L_q are microtubule lengths from spindle poles to the linked sites. In the third item, v_p and v_q are the relative velocities between the motor and the cross-linked microtubules.

On the other hand, the forces exerted on microtubules generated by motors (\mathbf{F}_{mo}) can be decomposed into the microtubule direction (f_r) and its normal direction (f^*) [50]. Therefore [50],

$$\mathbf{F}_{\text{mo}} = (f_r^\pm)_p \mathbf{r}_p + f_p^* \mathbf{r}_p^* = (f_r^\pm)_q \mathbf{r}_q + f_q^* \mathbf{r}_q^*. \quad (\text{B10})$$

Here, the forces generated by motors walking along the antiparallel microtubules (f_r^\pm) are also velocity dependent and given by [50] $(f_r^\pm)_p = f_0^\pm (1 \pm v_p/v_0^\pm)$ and $(f_r^\pm)_q = f_0^\pm (1 \pm v_q/v_0^\pm)$, where the positive directions of v_p and v_q are along the minus end of the microtubules. The plus sign represents the pushing force generated by kinesin, and the minus sign represents the pulling force generated by dynein. The normal components f_p^* and f_q^* can drive the rotation of the microtubules and be written as [50] $f_p^* = \omega_p \xi l_p L_p$ and $f_q^* = \omega_q \xi l_q L_q$, where ω_p and ω_q are the angular velocities of the microtubules, ξ is the rotary resistance coefficient of the microtubule with unit length, and l_p and l_q are the total microtubule lengths.

Taken together, Eqs. (B9) and (B10) can be solved when decomposed into the x and y directions, and hence four unknowns (ϕ_p , ϕ_q , v_p , and v_q) are obtained. Based on these motor velocities, we can solve the interactional forces on the pair of antiparallel microtubules. Notice that if the pushing force reaches the Euler buckling force, the force equals the buckling force, and the length in the Euler buckling formula is the microtubule length from the spindle pole to the linked site (i.e., L_p or L_q). In addition, the cross-linker motors bound to microtubules can also unbind at load-dependent rates just as in Eqs. (B3) and (B5).

7. Cohesion force between poles

The spindle pole is usually constituted of one centrosome containing a pair of centrioles surrounded by pericentriolar material (PCM) [105]. The integrity of the spindle pole relies on the connection between the centriole pair [106,107], which is established during the S phase and

persists for the entire mitosis [6]. However, abnormal force generated by mitotic proteins such as separase [108,109] might result in premature centriole disengagement and the subsequent formation of multipolar spindles. Additionally, the integrity of the spindle pole is also ensured by a complex network of both PCM and pericentriolar satellite proteins [6], which includes the recruitment and turnover of centrosomal proteins [110–112]. Ninein at pericentriolar satellites may anchor microtubules during the interphase [113,114]. In fact, the depletion of ninein or other pericentriolar satellite proteins can lead to PCM fragmentation, followed by the formation of multipolar spindles [112,115–120]. Recently, many centriole (e.g., CEP63) and PCM proteins (e.g., CNN/CDK5RAP2) that sustain the cohesion of spindle poles are identified [121–124]. Taken together, proteins that maintain the stability of the centriole pair and PCM-pericentriolar satellite networks provide the cohesion force to ensure the structural integrity of spindle poles [6,124]. Furthermore, the cohesion force of functional spindle poles must be able to resist the pulling and pushing forces generated by dynein and Eg5 (kinesin-5) acting on microtubules to drive pole fragmentation during spindle formation [6,107].

To consider the splitting and clustering of any two spindle poles, we define a cohesion force between any two poles as

$$F_c = \begin{cases} -AL_{ij}(L_{ij} - L_c)^2 & \text{for } L_{ij} \leq L_c \\ 0 & \text{for } L_{ij} > L_c, \end{cases} \quad (\text{B11})$$

where L_{ij} is the distance between the two poles, L_c represents the range of cohesion force, and A is a constant. In the simulation, we assume $L_c = 2 \mu\text{m}$ and $A = 80 \text{ pN}/(\mu\text{m})^3$. This force tends to maintain the structural integrity of the spindle pole under external forces [6].

8. Anti-overlapping force

The spindle poles and chromosomes do not penetrate the cell cortex and are confined in the cell. Furthermore, chromosomes cannot overlap with each other or with spindle poles [42,49–51]. To prevent the overlap or penetration, the short-range repulsive force is defined between any two objects, including centrosomes, chromosomes, and the cell cortex, except for any two poles,

$$F_v = \begin{cases} B(1/d - 1/d_0) & \text{for } d \leq d_0 \\ 0 & \text{for } d > d_0, \end{cases} \quad (\text{B12})$$

where d is the least distance between the two objects, d_0 is the range of anti-overlapping force, and B is a constant. In the simulation, we assume $d_0 = 1 \mu\text{m}$ and $B = 200 \text{ pN} \cdot \mu\text{m}$.

9. Motions of spindle poles and chromosomes

Various forces exerted on the microtubules can be transferred to spindle poles. Therefore, the force balance equation of a spindle pole is given as [50]

$$\sum \mathbf{f}^{\pm} + \sum \mathbf{f}_c^+ + \sum \mathbf{f}_k^- + \sum \mathbf{f}_r^{\pm} + \sum \mathbf{F}_c + \sum \mathbf{F}_v + \xi_p \mathbf{V} = 0. \quad (\text{B13})$$

Here, the first four items represent the forces of the microtubules nucleated at this spindle pole; the fifth item denotes the cohesion force between poles; the sixth item denotes the anti-overlapping forces; the last item denotes the viscous drag of the cytoplasm exerted on the pole, where ξ_p is the coefficient of the viscous drag and \mathbf{V} is the velocity of the pole. Notice that the inertial forces have been neglected due to the low Reynolds number in the system [50].

Chromosomes are regarded as a rigid rod. Similarly, the force balance equations of a chromosome are given by [50]

$$\sum \mathbf{f}_c^+ + \sum \mathbf{f}_k^- + \sum \mathbf{F}_v + \xi_c \mathbf{V}_c = 0, \quad (\text{B14})$$

$$\sum \mathbf{f}_c^+ \times \mathbf{r}_b + \sum \mathbf{f}_k^- \times \mathbf{r}_b + \zeta_c \dot{\Theta} = 0. \quad (\text{B15})$$

Here, \mathbf{r}_b is the vector from the center of the chromosome to the binding site; \mathbf{V}_c is the velocity of the centroid of the chromosome; Θ is the direction angle of the chromosome; ξ_c and ζ_c are the coefficients of translational and rotational viscous drag of the chromosome, respectively. For simplicity, the circumference of the chromosome is defined as its boundary for calculating the minimal distance of the anti-overlapping force; hence, the anti-overlapping force does not lead to a torque exerted on the chromosome [50].

10. Simulation method and results

As the initial condition, we consider four spindle poles, among which one pair of poles is clustered together initially, and the initial positions of these poles are randomly distributed inside the cell [Fig. 4(a) in the main text]. Therefore, we can investigate the clustering and splitting of spindle poles. The parameters used in the simulation are summarized in Table I.

Our numerical simulations demonstrate that the fraction of pole splitting increases in round cells (aspect ratio = 1), in comparison with elongated cells (aspect ratio = 3) [Fig. 4(b) in the main text]. In contrast, pole clustering is more frequent in elongated cells than that in round cells [Fig. 4(b) in the main text]. These results further confirm our experimental observations [Fig. 2(i) in the main text] and are also consistent with previous studies. Extra centrosomes can be separated by the pushing force generated by cross-linked kinesin-5 on the microtubules [107].

TABLE I. Parameters used in the simulation.

Parameter	Description
Geometric parameters	
$D_{\text{cell}} = 23 \mu\text{m}$	Diameter of the cell
$\lambda = 1 \sim 5$	The aspect ratio of the cell. It is defined as the ratio of the long axis to the short axis.
$L_{\text{ch}} = 2.5 \mu\text{m}$	Length of the chromosome [50]
$L_{\text{kine}} = L_{\text{ch}}/5$	Size of the kinetochore [50]
Microtubule dynamics	
$v_1 = 0.12 \mu\text{m/s}$	Free polymerization rate (growing velocity) of microtubules [79,125–128]
$v_2 = 0.25 \mu\text{m/s}$	Free depolymerization rate (shrinking velocity) of microtubules [79,125–128]
$k_1 = 0.04 \text{ s}^{-1}$	Rescue rate of microtubules (from shrinking to growing) [79,125,127,128]
$k_2 = 0.02 \text{ s}^{-1}$	Catastrophe rate of microtubules (from growing to shrinking) [79,125,127,128]
$k_2^* = 0.03 \text{ s}^{-1}$	Catastrophe rate of microtubules stopped by the cell cortex [43]
$k_0 = 3 \text{ s}^{-1}$	Nucleation rate of microtubules from one centrosome [79,80,89,90]
$k_n = 2$	Additional nucleation rate coefficient of microtubules from one centrosome to all chromosomes [42]
$k_l = 0.015$	Additional nucleation rate of bundle microtubules, estimation
$\kappa = 33.12 \text{ pN} \cdot \mu\text{m}^2$	Bending rigidity of microtubules [87]
$f_{\text{stall}} = 50 \text{ pN}$	Stall force of microtubule polymerization [80,129]
$f_{k,0} = 1 \text{ pN}/\mu\text{m}$	Depolymerization force of unit-length microtubule at the kinetochore [85,100,101]
$\xi = 1000 \text{ pN} \cdot \text{s}/\mu\text{m}^2$	Friction coefficient of microtubule rotation [80,89]
Molecular motor dynamics	
$k_b^- = 0.02 \text{ s}^{-1}$	Binding rate of cortical dynein [79,89,130]
$k_{b,c} = 0.05 \text{ s}^{-1}$	Binding rate of chromokinesin [85,97,131]
$k_{b,k} = 0.08 \text{ s}^{-1}$	Binding rate of kinetochore [85,97,131]
$k_{b,r}^+ = 0.05 \text{ s}^{-1}$	Binding rate of kinesin as cross-linkers [132,133]
$k_{b,r}^- = 0.01 \text{ s}^{-1}$	Binding rate of dynein as cross-linkers [132,133]
$f_0^+ = 5 \text{ pN}$	Stall force of kinesin [134,135]
$f_0^- = 5 \text{ pN}$	Stall force of dynein [128,134]
$v_0^+ = 0.2 \mu\text{m/s}$	Unloaded velocity of kinesin [134,135]
$v_0^- = 0.2 \mu\text{m/s}$	Unloaded velocity of dynein [128,134]

(Table continued)

TABLE I. (*Continued*)

Parameter	Description
$k_0^+ = 0.01 \text{ s}^{-1}$	Unloaded unbinding rate of kinesin [85,97,131]
$k_0^- = 0.02 \text{ s}^{-1}$	Unloaded unbinding rate of dynein [79,89,130]
$k_{0,k}^- = 0.005 \text{ s}^{-1}$	Unloaded unbinding rate of kinetochore [85,100]
$f_u^+ = 20 \text{ pN}$	Characteristic force representing the sensitivity of the unbinding rate of kinesin to the load [97,132]
$f_u^- = 20 \text{ pN}$	Characteristic force representing the sensitivity of the unbinding rate of dynein or kinetochore to the load [89,132]
$\eta = 0.01 \text{ pN}/\mu\text{m}$	Cytoplasmic pulling force per unit microtubule length, estimated in Ref. [42]
Centrosome and chromosome dynamics	
$\xi_p = 10 \text{ pN} \cdot \text{s}/\text{nm}$	Viscous drag coefficient of centrosome, estimated in Ref. [42]
$\xi_c = 30 \text{ pN} \cdot \text{s}/\text{nm}$	Translational viscous drag coefficient of chromosome, estimated in Ref. [42]
$\zeta_c = 1255.5 \text{ pN} \cdot \text{s} \cdot \text{nm}$	Rotational viscous drag coefficient of chromosome, estimated in Ref. [42]

On the contrary, the pulling force generated by cross-linked dyneins and kinetochore microtubules can promote the coalescence of the extra centrosomes [15,17,124]. Our results suggest that the behavior of multipolar spindles, including pole splitting and clustering, could be linked to the microtubule-related forces regulated by the cell shape.

Interestingly, our simulation also predicts that the cell shape effectively regulates the configuration of multipolar spindles (Fig. 10). The multipolar spindle will change from a regular polygon to a chain of smaller bipolar spindles when the aspect ratio of the cell shape increases.

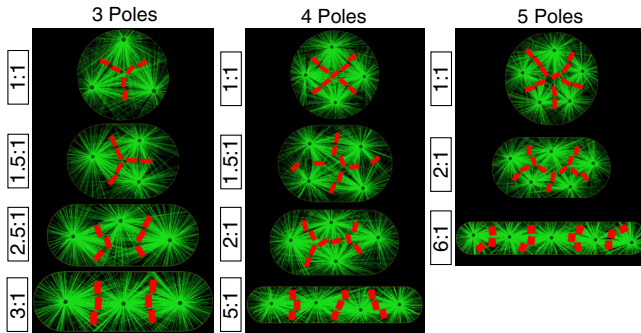


FIG. 10. Four-wall confinement changing cell shape, which in turn effectively regulates the configuration of multipolar spindles. The multipolar spindles will change from regular polygons to a chain of smaller bipolar spindles when the aspect ratio of the cell shape increases.

APPENDIX C: THEORETICAL MODEL

To get more insight about how mechanical confinement regulates the configuration, and pole splitting and clustering of multipolar spindles, we develop a simplified theory based on the interacting particle model [51,54] [Fig. 5(a) in the main text], in which spindle poles are considered particles interacting with each other by pairwise interactions (pole-pole interaction), and interactions exist between each spindle pole and the cell boundary (pole-cortex interaction). Therefore, the movement, positioning, splitting, and clustering of spindle poles are governed by the competition between the pole-pole interaction and the pole-cortex interaction [16]. The superposition of the pole-pole interaction and the pole-cortex interaction yields the total energy of the system as

$$E = E_{p-p} + E_{c-p} = \sum_{i,j=1}^n E_{p-p}^{ij} + \sum_{i=1}^n E_{c-p}^i, \quad (\text{C1})$$

where E_{p-p} represents the total energy of n poles due to the pole-pole interaction, E_{p-p}^{ij} is the pairwise pole-pole interaction between the i th and the j th poles ($i, j = 1, 2, \dots, n$), E_{c-p} denotes the total pole-cortex interaction, and E_{c-p}^i is the pole-cortex interaction between the i th pole and the cortex.

1. Pole-pole interaction

In the absence of the cortex, the interaction force between two poles F_{p-p}^{ij} as a function of pole-pole distance L_{ij} can be calculated in our simulation [Fig. 5(c) in the main text], which can be well fitted by the following equation:

$$F_{p-p}^{ij} = (aL_{ij}^3 + bL_{ij}^2 + cL_{ij})e^{-L_{ij}/L_{pp}}, \quad (\text{C2})$$

which satisfies the requirement of the interaction force between two poles: $F_{p-p}^{ij} = 0$ when $L_{ij} = 0$, and $F_{p-p}^{ij} \rightarrow 0$ as $L_{ij} \rightarrow \infty$. The integration of this fitted interaction force yields the pairwise pole-pole interaction energy. Specifically, the change of potential energy by increasing the distance between the two poles from L_{ij} to ∞ is [51]

$$E_{p-p}^{ij}|_{L_{ij}}^{\infty} = - \int_{L_{ij}}^{\infty} F_{p-p}^{ij} dL_{ij}. \quad (\text{C3})$$

Noticing $E_{p-p}^{ij} = 0$ at $L_{ij} \rightarrow \infty$, we obtain the pairwise pole-pole interaction energy as

$$\begin{aligned} E_{p-p}^{ij} &= \int_{L_{ij}}^{\infty} F_{p-p}^{ij} dL_{ij} \\ &= [aL_{pp}L_{ij}^3 + (3aL_{pp}^2 + bL_{pp})L_{ij}^2 \\ &\quad + (6aL_{pp}^3 + 2bL_{pp}^2 + cL_{pp})L_{ij} \\ &\quad + (6aL_{pp}^4 + 2bL_{pp}^3 + cL_{pp}^2)]e^{-L_{ij}/L_{pp}}, \end{aligned} \quad (\text{C4})$$

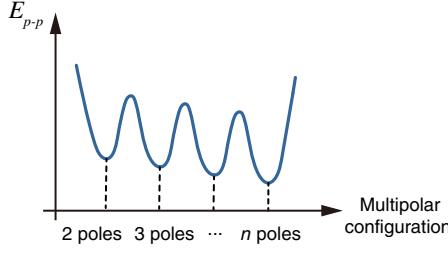


FIG. 11. Total pole-pole energy landscape of multiple poles.

which is a double-well potential [51,55–57] with two minima representing two stable states, i.e., the clustered and split states of the two poles [see Fig. 5(d) in the main text]. This is strongly reminiscent of a reversible chemical reaction, where the splitting reaction and clustering reaction should overcome energy barriers ΔE_{split} and $\Delta E_{\text{cluster}}$, respectively [Fig. 5(d) in the main text]. If there are n spindle poles, the total pole-pole energy should be a multiple-well potential with many metastable spindle configurations (Fig. 11).

2. Pole-cortex interaction

Both the pushing force and pulling force can be generated between the cell cortex and the spindle poles due to the growth of microtubules and the walking of molecular motors, so the spindle can be positioned and oriented [42,49,50,88,89,136].

In our theoretical model, we assume that the angular densities of pushing and pulling microtubules are n^+ and n^- , respectively [80,89]. Similar to our simulation, the pushing force of a single microtubule is given as $f^+ = \pi^2 \kappa / l^2$, where κ denotes the bending rigidity and l denotes the microtubule length [42,43,50,58,80,89]. Additionally, the pulling force exerted on microtubules is generated by cortical dynein [85,91]. Dynein walks to the minus end of the microtubule and thus generates a pulling force on the microtubule [85,89,92–94]. The pulling force of a single microtubule f^- can be described by $f^- = f_0 e^{-l/L_0}$ [51], where f_0 is a constant and L_0 is the average range of the attraction to the cortex. Therefore, the pole-cortex interaction between the i th pole and the cortex E_{c-p}^i can be obtained by calculating the work done by the pulling and pushing forces when proportionally enlarging the cell from the current size to infinity [51] as

$$E_{c-p}^i \Big|_{\text{current size}}^{\infty} = - \oint \left(\int_{\rho_i}^{\infty} (n^+ f^+ - n^- f^-) dl \right) d\phi, \quad (\text{C5})$$

where ρ_i is the distance from the i th pole to the cortex in the ϕ direction. Notice that E_{c-p}^i should be zero when the cell is infinitely large. Thus, we have

TABLE II. Parameters used in the theoretical model.

Parameter	Description
$a = -5.5 \text{ pN}/(\mu\text{m})^3$	
$b = 94.05 \text{ pN}/(\mu\text{m})^2$	Fitting parameters of the pairwise pole-pole force based on our simulation
$c = -207.35 \text{ pN}/\mu\text{m}$	The distance of two poles in the split state is a typical spindle length (about $15 \mu\text{m}$) based on our experiments and the literature [42,47].
$L_{pp} = 5.128 \mu\text{m}$	
$n^+ = 10/(2\pi)$	Angular densities of pushing microtubules, estimated from Refs. [80,89]
$n^- = 10/(2\pi)$	Angular densities of pulling microtubules, estimated from Refs. [80,89]
$\kappa = 33.12 \text{ pN} \cdot \mu\text{m}^2$	Bending rigidity of microtubules, taken from Ref. [87]
$f_0 = 5 \text{ pN}$	Amplitude of pole-cortex pulling force, taken from Refs. [80,89,137]
$L_0 = 10 \mu\text{m}$	Average range of the pulling interaction of the cortex, estimated from Ref. [51]

$$\begin{aligned} E_{c-p}^i &= \oint d\phi \int_{\rho_i}^{\infty} \left(n^+ \frac{\pi^2 \kappa}{l^2} - n^- f_0 e^{-l/L_0} \right) dl \\ &= \int_0^{2\pi} \left(n^+ \frac{\pi^2 \kappa}{\rho_i} - n^- f_0 L_0 e^{-\rho_i/L_0} \right) d\phi. \end{aligned} \quad (\text{C6})$$

From Eq. (C6), we can see that the pole-cortex interaction (E_{c-p}^i) depends on the distance between the pole and the cortex; i.e., the pole-cortex interaction becomes more repulsive when the pole approaches the cortex, and it diminishes when the pole retreats from the cortex [Fig. 5(b) in the main text]. The parameters used in the pole-cortex interaction are listed in Table II.

It is difficult to obtain the pole-cortex interaction potential in most cases. Next, we analyze the pole-cortex interaction under two simple conditions, i.e., the round cell and elongated cell with a stadium shape.

a. Pole-cortex interaction in round cells

In the absence of lateral confinement in wide microchannels, the cell is round with a radius of R . The origin of the coordinate system is at the cell center, and the coordinates of the i th pole are (x_i, y_i) (Fig. 12). The distance between the pole and the cortex in the direction of ϕ is easier to obtain in the polar coordinate system, where the origin of the polar coordinate is at the position of the pole (x_i, y_i) (Fig. 12).

Thus, the equation of the cortex could be described as

$$\rho_i^2 - 2r_1 \cdot \rho_i \cdot \cos \phi + r_1^2 - R^2 = 0, \quad (\text{C7})$$

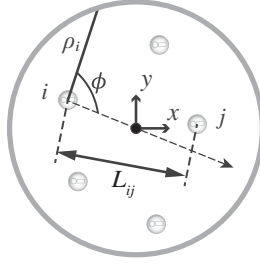


FIG. 12. Schematic diagram of the pole-pole interaction and the pole-cortex interaction in a round cell. Note that L_{ij} is the distance between any two poles, and ρ_i is the distance from the i th pole to the cortex in the ϕ direction.

where $r_1 = \sqrt{x_i^2 + y_i^2}$. Therefore, the distance between the pole and the cortex is

$$\rho_i(\phi) = r_1 \cdot \cos \phi + \sqrt{R^2 - r_1^2 \cdot \sin^2 \phi}. \quad (\text{C8})$$

After substituting ρ_i into Eq. (C6), we have the pole-cortex interaction potential in round cells.

b. Pole-cortex interaction in elongated cells

The cells under the four-wall confinement are regarded as a stadium shape with two semicircular ends (Fig. 13). In this case, Eq. (C6) consists of four parts:

$$E_{c-p}^i = \sum_{k=1}^4 E_{c,k}^i = E_{c,1}^i + E_{c,2}^i + E_{c,3}^i + E_{c,4}^i, \quad (\text{C9})$$

where

$$\begin{aligned} E_{c,1}^i &= \int_{\phi_1}^{\phi_2} \left(n^+ \frac{\pi^2 \kappa}{\rho_i} - n^- f_0 L_0 e^{-\rho_i/L_0} \right) d\phi, \\ E_{c,2}^i &= \int_{\phi_2}^{\phi_3} \left(n^+ \frac{\pi^2 \kappa}{\rho_i} - n^- f_0 L_0 e^{-\rho_i/L_0} \right) d\phi, \\ E_{c,3}^i &= \int_{\phi_3}^{\phi_4} \left(n^+ \frac{\pi^2 \kappa}{\rho_i} - n^- f_0 L_0 e^{-\rho_i/L_0} \right) d\phi, \\ E_{c,4}^i &= \int_{\phi_4}^{\phi_5} \left(n^+ \frac{\pi^2 \kappa}{\rho_i} - n^- f_0 L_0 e^{-\rho_i/L_0} \right) d\phi. \end{aligned} \quad (\text{C10})$$

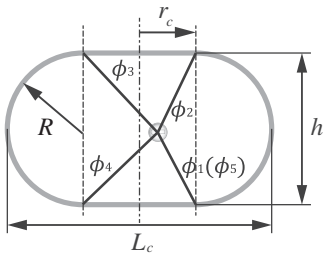


FIG. 13. Cell under four-wall confinement regarded as a stadium shape with two semicircular ends. For the sake of calculation, the cell is divided into four parts.

The first part ($\phi_1 \sim \phi_2$) and the third part ($\phi_3 \sim \phi_4$) are semicircular, while the other two parts ($\phi_2 \sim \phi_3$ and $\phi_4 \sim \phi_5$) are straight, where ϕ_5 returns to the position of ϕ_1 (Fig. 13).

For the two semicircle parts, we also use a polar coordinate. Their radius is $R = h/2$, and their centers are $(r_c, 0)$ and $(-r_c, 0)$. We also define the i th pole position (x_i, y_i) as the origin of the polar coordinate, and $\rho_i(\phi)$ follows:

$$\rho_i(\phi) = r_2 \cdot \cos \phi + \sqrt{R^2 - r_2^2 \cdot \sin^2 \phi}, \quad (\text{C11})$$

where

$$r_2 = \begin{cases} \sqrt{(x_i - r_c)^2 + y_i^2} & \phi_1 < \phi < \phi_2 \\ \sqrt{(x_i + r_c)^2 + y_i^2} & \phi_3 < \phi < \phi_4. \end{cases} \quad (\text{C12})$$

The angles ϕ_1 , ϕ_2 , ϕ_3 , and ϕ_4 are variable when the position of the pole is different. To simplify the calculation of these angles, we set up two different coordinate systems. For the first part ($\phi_1 \sim \phi_2$), the polar axis of the polar coordinate is along $\mathbf{n} = (r_c - x_i, -y_i)$, while for the third part ($\phi_3 \sim \phi_4$), the polar axis is along $\mathbf{n} = (-r_c - x_i, -y_i)$. The direction vectors corresponding to ϕ_1 , ϕ_2 , ϕ_3 , and ϕ_4 are $\mathbf{n}_1 = (r_c - x_i, -R - y_i)$, $\mathbf{n}_2 = (r_c - x_i, R - y_i)$, $\mathbf{n}_3 = (-r_c - x_i, R - y_i)$, and $\mathbf{n}_4 = (-r_c - x_i, -R - y_i)$, respectively. Therefore, the angles ϕ_1 , ϕ_2 , ϕ_3 , and ϕ_4 are given in Table III.

Therefore, substituting the angles ϕ_1 , ϕ_2 , ϕ_3 , and ϕ_4 into Eq. (C10), we derive the contribution of the two semicircular parts of the cortex, i.e., $E_{c,1}^i$ and $E_{c,3}^i$ [Eq. (C9)].

Next, we try to calculate $E_{c,2}^i$ and $E_{c,4}^i$. For the straight parts, the cortex equation is $y = \pm R$, and the expression of ρ_i is given by

TABLE III. Angles $\phi_1 \sim \phi_4$ for calculating the semicircular parts.

	ϕ_1	ϕ_2	ϕ_3	ϕ_4
$x_i \leq -r_c$	$-\langle \mathbf{n}, \mathbf{n}_1 \rangle^a$	$\langle \mathbf{n}, \mathbf{n}_2 \rangle$	$\langle \mathbf{n}, \mathbf{n}_3 \rangle$	$2\pi - \langle \mathbf{n}, \mathbf{n}_4 \rangle$
$-r_c < x_i < r_c$	$-\langle \mathbf{n}, \mathbf{n}_1 \rangle$	$\langle \mathbf{n}, \mathbf{n}_2 \rangle$	$-\langle \mathbf{n}, \mathbf{n}_3 \rangle$	$\langle \mathbf{n}, \mathbf{n}_4 \rangle$
$x_i \geq r_c$	$\langle \mathbf{n}, \mathbf{n}_1 \rangle$	$2\pi - \langle \mathbf{n}, \mathbf{n}_2 \rangle$	$-\langle \mathbf{n}, \mathbf{n}_3 \rangle$	$\langle \mathbf{n}, \mathbf{n}_4 \rangle$

^a $\langle \mathbf{n}, \mathbf{n}_1 \rangle$ represents the angle between the two vectors.

TABLE IV. Angles $\phi_2 \sim \phi_5$ for calculating the straight parts.

ϕ_2	ϕ_3	ϕ_4	ϕ_5
$\langle \mathbf{n}_2, \mathbf{x} \rangle^a$	$\langle \mathbf{n}_3, \mathbf{x} \rangle$	$2\pi - \langle \mathbf{n}_4, \mathbf{x} \rangle$	$2\pi - \langle \mathbf{n}_5, \mathbf{x} \rangle^b$

^a \mathbf{x} represents the x axis, i.e., $\mathbf{x} = (1, 0)$.

^b $\mathbf{n}_5 = \mathbf{n}_1$.

$$\rho_i(\phi) = \begin{cases} (R - y_i)/\sin\phi & \phi_2 < \phi < \phi_3 \\ (-R - y_i)/\sin\phi & \phi_4 < \phi < \phi_5. \end{cases} \quad (\text{C13})$$

Here, $\phi_2 \sim \phi_5$ is given in Table IV.

Therefore, we have derived the two straight parts of the cortex, $E_{c,2}^i$ and $E_{c,4}^i$. Taken together, the pole-cortex interaction potential in elongated cells [Eq. (C9)] has been completely solved.

Based on experimental data, we can acquire the parameters such as the distance between any two poles (L_{ij}) and cell shape (L_c , r_c , h , and R). Thus, we can calculate the pole-pole interaction (E_{p-p}), the pole-cortex interaction (E_{c-p}), and the total energy of the system (E) during the process of pole clustering and pole splitting.

- [1] C. Lengauer, K. W. Kinzler, and B. Vogelstein, *Genetic Instability in Colorectal Cancers*, *Nature (London)* **386**, 623 (1997).
- [2] E. A. Nigg, *Centrosome Aberrations: Cause or Consequence of Cancer Progression?*, *Nat. Rev. Cancer* **2**, 815 (2002).
- [3] R. A. Burrell, N. McGranahan, J. Bartek, and C. Swanton, *The Causes and Consequences of Genetic Heterogeneity in Cancer Evolution*, *Nature (London)* **501**, 338 (2013).
- [4] N. J. Ganem, S. A. Godinho, and D. Pellman, *A Mechanism Linking Extra Centrosomes to Chromosomal Instability*, *Nature (London)* **460**, 278 (2009).
- [5] A. W. Duncan, M. H. Taylor, R. D. Hickey, A. E. H. Newell, M. L. Lenzi, S. B. Olson, M. J. Finegold, and M. Grompe, *The Ploidy Conveyor of Mature Hepatocytes as a Source of Genetic Variation*, *Nature (London)* **467**, 707 (2010).
- [6] H. Maiato and E. Logarinho, *Mitotic Spindle Multipolarity without Centrosome Amplification*, *Nat. Cell Biol.* **16**, 386 (2014).
- [7] A. W. Duncan, A. E. H. Newell, L. Smith, E. M. Wilson, S. B. Olson, M. J. Thayer, S. C. Strom, and M. Grompe, *Frequent Aneuploidy Among Normal Human Hepatocytes*, *Gastroenterology* **142**, 25 (2012).
- [8] K. A. Knouse, K. E. Lopez, M. Bachofner, and A. Amon, *Chromosome Segregation Fidelity in Epithelia Requires Tissue Architecture*, *Cell* **175**, 200 (2018).
- [9] T. Boveri, *The Origin of Malignant Tumors* (Williams and Wilkins, Baltimore, 1929).
- [10] T. Fujiwara, M. Bandi, M. Nitta, E. V. Ivanova, R. T. Bronson, and D. Pellman, *Cytokinesis Failure Generating Tetraploids Promotes Tumorigenesis in p53-Null Cells*, *Nature (London)* **437**, 1043 (2005).
- [11] L. Cassimeris and J. Morabito, *TOGp, the Human Homolog of XMAP215/Dis1, Is Required for Centrosome Integrity, Spindle Pole Organization, and Bipolar Spindle Assembly*, *Mol. Biol. Cell* **15**, 1580 (2004).
- [12] M. De Luca, L. Brunetto, I. Asteriti, M. Giubettini, P. Lavia, and G. Guarguaglini, *Aurora-A and ch-TOG Act in a Common Pathway in Control of Spindle Pole Integrity*, *Oncogene* **27**, 6539 (2008).
- [13] N. Oshimori, M. Ohsugi, and T. Yamamoto, *The Plk1 Target Kizuna Stabilizes Mitotic Centrosomes to Ensure Spindle Bipolarity*, *Nat. Cell Biol.* **8**, 1095 (2006).
- [14] B. R. Brinkley, *Managing the Centrosome Numbers Game: From Chaos to Stability in Cancer Cell Division*, *Trends Cell Biol.* **11**, 18 (2001).
- [15] R. Basto, K. Brunk, T. Vinadogrova, N. Peel, A. Franz, A. Khodjakov, and J. W. Raff, *Centrosome Amplification Can Initiate Tumorigenesis in Flies*, *Cell* **133**, 1032 (2008).
- [16] M. Kwon, S. A. Godinho, N. S. Chandhok, N. J. Ganem, A. Azioune, M. Thery, and D. Pellman, *Mechanisms to Suppress Multipolar Divisions in Cancer Cells with Extra Centrosomes*, *Genes Dev.* **22**, 2189 (2008).
- [17] N. J. Quintyne, J. E. Reing, D. R. Hoffelder, S. M. Gollin, and W. S. Saunders, *Spindle Multipolarity Is Prevented by Centrosomal Clustering*, *Science* **307**, 127 (2005).
- [18] W. T. Silkworth, I. K. Nardi, L. M. Scholl, and D. Cimini, *Multipolar Spindle Pole Coalescence Is a Major Source of Kinetochore Mis-attachment and Chromosome Mis-segregation in Cancer Cells*, *PLoS One* **4**, e6564 (2009).
- [19] M. D. Vahey and D. A. Fletcher, *The Biology of Boundary Conditions: Cellular Reconstitution in One, Two, and Three Dimensions*, *Curr. Opin. Cell Biol.* **26**, 60 (2014).
- [20] A. J. Engler, S. Sen, H. L. Sweeney, and D. E. Discher, *Matrix Elasticity Directs Stem Cell Lineage Specification*, *Cell* **126**, 677 (2006).
- [21] M. Théry, V. Racine, A. Pépin, M. Piel, Y. Chen, J.-B. Sibarita, and M. Bornens, *The Extracellular Matrix Guides the Orientation of the Cell Division Axis*, *Nat. Cell Biol.* **7**, 947 (2005).
- [22] F. J. Segerer, F. Thüroff, A. P. Alberola, E. Frey, and J. O. Rädler, *Emergence and Persistence of Collective Cell Migration on Small Circular Micropatterns*, *Phys. Rev. Lett.* **114**, 228102 (2015).
- [23] L. Q. Wan, K. Ronaldson, M. Park, G. Taylor, Y. Zhang, J. M. Gimble, and G. Vunjak-Novakovic, *Micropatterned Mammalian Cells Exhibit Phenotype-Specific Left-Right Asymmetry*, *Proc. Natl. Acad. Sci. U.S.A.* **108**, 12295 (2011).
- [24] S. R. K. Vedula, M. C. Leong, T. L. Lai, P. Hensen, A. J. Kabla, C. T. Lim, and B. Ladoux, *Emerging Modes of Collective Cell Migration Induced by Geometrical Constraints*, *Proc. Natl. Acad. Sci. U.S.A.* **109**, 12974 (2012).
- [25] S. R. K. Vedula, H. Hirata, M. H. Nai, Y. Toyama, X. Trepat, C. T. Lim, B. Ladoux, *Epithelial Bridges Maintain Tissue Integrity During Collective Cell Migration*, *Nat. Mater.* **13**, 87 (2014).
- [26] A. Lomakin, C. Cattin, D. Cuvelier, Z. Alraies, M. Molina, G. Nader, N. Srivastava, P. Sáez, J. Garcia-Arcos, I. Zhitnyak *et al.*, *The Nucleus Acts as a Ruler Tailoring Cell Responses to Spatial Constraints*, *Science* **370**, eaba2894 (2020).
- [27] V. Venturini, F. Pezzano, F. Catala Castro, H.-M. Häkkinen, S. Jiménez-Delgado, M. Colomer-Rosell, M. Marro, Q. Tolosa-Ramon, S. Paz-López, M. A. Valverde *et al.*, *The Nucleus Measures Shape Changes for Cellular Proprioception to Control Dynamic Cell Behavior*, *Science* **370**, eaba2644 (2020).
- [28] K. A. Knouse, J. Wu, C. A. Whittaker, and A. Amon, *Single Cell Sequencing Reveals Low Levels of Aneuploidy*

- Across Mammalian Tissues*, *Proc. Natl. Acad. Sci. U.S.A.* **111**, 13409 (2014).
- [29] G. Helmlinger, P. A. Netti, H. C. Lichtenbeld, R. J. Melder, and R. K. Jain, *Solid Stress Inhibits the Growth of Multicellular Tumor Spheroids*, *Nat. Biotechnol.* **15**, 778 (1997).
- [30] T. Stylianopoulos, J. D. Martin, V. P. Chauhan, S. R. Jain, B. Diop-Frimpong, N. Bardeesy, B. L. Smith, C. R. Ferrone, F. J. Hornicek, Y. Boucher *et al.*, *Causes, Consequences, and Remedies for Growth-Induced Solid Stress in Murine and Human Tumors*, *Proc. Natl. Acad. Sci. U.S.A.* **109**, 15101 (2012).
- [31] T. P. Padera, B. R. Stoll, J. B. Tooredman, D. Capen, E. d. Tomaso, and R. K. Jain, *Cancer Cells Compress Intratumour Vessels*, *Nature (London)* **427**, 695 (2004).
- [32] O. M. Lancaster, M. Le Berre, A. Dimitracopoulos, D. Bonazzi, E. Zlotek-Zlotkiewicz, R. Picone, T. Duke, M. Piel, and B. Baum, *Mitotic Rounding Alters Cell Geometry to Ensure Efficient Bipolar Spindle Formation*, *Dev. Cell* **25**, 270 (2013).
- [33] H. T. K. Tse, W. M. Weaver, and D. Di Carlo, *Increased Asymmetric and Multi-daughter Cell Division in Mechanically Confined Microenvironments*, *PLoS One* **7**, e38986 (2012).
- [34] H. Kittur, W. Weaver, and D. Di Carlo, *Well-Plate Mechanical Confinement Platform for Studies of Mechanical Mutagenesis*, *Biomed. Microdevices* **16**, 439 (2014).
- [35] Z. Tong, E. M. Balzer, M. R. Dallas, W.-C. Hung, K. J. Stebe, and K. Konstantopoulos, *Chemotaxis of Cell Populations through Confined Spaces at Single-Cell Resolution*, *PLoS One* **7**, e29211 (2012).
- [36] K. M. Stroka, H. Jiang, S.-H. Chen, Z. Tong, D. Wirtz, S. X. Sun, and K. Konstantopoulos, *Water Permeation Drives Tumor Cell Migration in Confined Microenvironments*, *Cell* **157**, 611 (2014).
- [37] K. Xie, Y. Yang, and H. Jiang, *Controlling Cellular Volume via Mechanical and Physical Properties of Substrate*, *Biophys. J.* **114**, 675 (2018).
- [38] See Supplemental Material at <http://link.aps.org/supplemental/10.1103/PhysRevX.13.011036> for [brief description].
- [39] B. Brinkley and P. N. Rao, *Nitrous Oxide: Effects on the Mitotic Apparatus and Chromosome Movement in HeLa Cells*, *J. Cell Biol.* **58**, 96 (1973).
- [40] A. Goupil, M. Nano, G. Letort, S. Gemble, F. Edwards, O. Goundiam, D. Gogendeau, C. Penetier, and R. Basto, *Chromosomes Function as a Barrier to Mitotic Spindle Bipolarity in Polyploid Cells*, *J. Cell Biol.* **219** (2020).
- [41] Z. Yang, J. Lončarek, A. Khodjakov, and C. L. Rieder, *Extra Centrosomes and/or Chromosomes Prolong Mitosis in Human Cells*, *Nat. Cell Biol.* **10**, 748 (2008).
- [42] J. Li and H. Jiang, *Geometric Asymmetry Induces Upper Limit of Mitotic Spindle Size*, *Biophys. J.* **112**, 1503 (2017).
- [43] H. Jiang, *Cell Size Modulates Oscillation, Positioning and Length of Mitotic Spindles*, *Sci. Rep.* **5**, 10504 (2015).
- [44] Y.-J. Liu, M. Le Berre, F. Lautenschlaeger, P. Maiuri, A. Callan-Jones, M. Heuzé, T. Takaki, R. Voituriez, and M. Piel, *Confinement and Low Adhesion Induce Fast Amoeboid Migration of Slow Mesenchymal Cells*, *Cell* **160**, 659 (2015).
- [45] C. J. Cattin, M. Düggelin, D. Martinez-Martin, C. Gerber, D. J. Müller, and M. P. Stewart, *Mechanical Control of Mitotic Progression in Single Animal Cells*, *Proc. Natl. Acad. Sci. U.S.A.* **112**, 11258 (2015).
- [46] V. Magidson, C. B. O'Connell, J. Lončarek, R. Paul, A. Mogilner, and A. Khodjakov, *The Spatial Arrangement of Chromosomes During Prometaphase Facilitates Spindle Assembly*, *Cell* **146**, 555 (2011).
- [47] W. Xi, C. K. Schmidt, S. Sanchez, D. H. Gracias, R. E. Carazo-Salas, R. Butler, N. Lawrence, S. P. Jackson, and O. G. Schmidt, *Molecular Insights into Division of Single Human Cancer Cells in On-Chip Transparent Microtubes*, *ACS Nano* **10**, 5835 (2016).
- [48] C. Cadart, E. Zlotek-Zlotkiewicz, M. Le Berre, M. Piel, and H. K. Matthews, *Exploring the Function of Cell Shape and Size During Mitosis*, *Dev. Cell* **29**, 159 (2014).
- [49] J. Li and H. Jiang, *Regulating Positioning and Orientation of Mitotic Spindles via Cell Size and Shape*, *Phys. Rev. E* **97**, 012407 (2018).
- [50] J. Li, L. Cheng, and H. Jiang, *Cell Shape and Intercellular Adhesion Regulate Mitotic Spindle Orientation*, *Mol. Biol. Cell* **30**, 2458 (2019).
- [51] S. Chatterjee, A. Sarkar, J. Zhu, A. Khodjakov, A. Mogilner, and R. Paul, *Mechanics of Multicentrosomal Clustering in Bipolar Mitotic Spindles*, *Biophys. J.* **119**, 434 (2020).
- [52] C. E. Miles, J. Zhu, and A. Mogilner, *Mechanical Torque Promotes Bipolarity of the Mitotic Spindle through Multicentrosomal Clustering*, *Bull. Math. Biol.* **84**, 1 (2022).
- [53] N. C. Baudoin, J. M. Nicholson, K. Soto, O. Martin, J. Chen, and D. Cimini, *Asymmetric Clustering of Centrosomes Defines the Early Evolution of Tetraploid Cells*, *eLife* **9**, e54565 (2020).
- [54] A. Manhart, S. Windner, M. Baylies, and A. Mogilner, *Mechanical Positioning of Multiple Nuclei in Muscle Cells*, *PLoS Comput. Biol.* **14**, e1006208 (2018).
- [55] P. Zhou and T. Li, *Construction of the Landscape for Multistable Systems: Potential Landscape, Quasi-potential, A-type Integral and Beyond*, *J. Chem. Phys.* **144**, 094109 (2016).
- [56] S. Curilef, C. Zander, and A. Plastino, *Two Particles in a Double Well: Illustrating the Connection between Entanglement and the Speed of Quantum Evolution*, *Eur. J. Phys.* **27**, 1193 (2006).
- [57] P. Zhou, X. Gao, X. Li, L. Li, C. Niu, Q. Ouyang, H. Lou, T. Li, and F. Li, *Stochasticity Triggers Activation of the S-phase Checkpoint Pathway in Budding Yeast*, *Phys. Rev. X* **11**, 011004 (2021).
- [58] J. Howard, *Elastic and Damping Forces Generated by Confined Arrays of Dynamic Microtubules*, *Phys. Biol.* **3**, 54 (2006).
- [59] R. Ma, L. Laan, M. Dogterom, N. Pavin, and F. Jülicher, *General Theory for the Mechanics of Confined Microtubule Asters*, *New J. Phys.* **16**, 013018 (2014).
- [60] C. Garzon-Coral, H. A. Fantana, and J. Howard, *A Force-Generating Machinery Maintains the Spindle at the Cell Center During Mitosis*, *Science* **352**, 1124 (2016).
- [61] T. Kiyomitsu and I. M. Cheeseman, *Chromosome- and Spindle-Pole-Derived Signals Generate an Intrinsic Code*

- for Spindle Position and Orientation, *Nat. Cell Biol.* **14**, 311 (2012).
- [62] T. Kiyomitsu and I. M. Cheeseman, *Cortical Dynein and Asymmetric Membrane Elongation Coordinately Position the Spindle in Anaphase*, *Cell* **154**, 391 (2013).
- [63] J. Fink, N. Carpi, T. Betz, A. Bétard, M. Chebah, A. Azioune, M. Bornens, C. Sykes, L. Fetler, D. Cuvelier *et al.*, *External Forces Control Mitotic Spindle Positioning*, *Nat. Cell Biol.* **13**, 771 (2011).
- [64] F. Lázaro-Diéguez, I. Ispolatov, and A. Müsch, *Cell Shape Impacts on the Positioning of the Mitotic Spindle with Respect to the Substratum*, *Mol. Biol. Cell* **26**, 1286 (2015).
- [65] J.-G. Chen and S. B. Horwitz, *Differential Mitotic Responses to Microtubule-Stabilizing and -Destabilizing Drugs*, *Cancer Res.* **62**, 1935 (2002).
- [66] J. Rosenblatt, L. P. Cramer, B. Baum, and K. M. McGee, *Myosin II-Dependent Cortical Movement Is Required for Centrosome Separation and Positioning During Mitotic Spindle Assembly*, *Cell* **117**, 361 (2004).
- [67] M. J. Bissell and W. C. Hines, *Why Don't We Get More Cancer? A Proposed Role of the Microenvironment in Restraining Cancer Progression*, *Nat. Medicine* **17**, 320 (2011).
- [68] C. M. Nelson and M. J. Bissell, *Of Extracellular Matrix, Scaffolds, and Signaling: Tissue Architecture Regulates Development, Homeostasis, and Cancer*, *Annu. Rev. Cell Dev. Biol.* **22**, 287 (2006).
- [69] D. S. Dolberg and M. J. Bissell, *Inability of Rous Sarcoma Virus to Cause Sarcomas in the Avian Embryo*, *Nature (London)* **309**, 552 (1984).
- [70] A. W. Stoker, C. Hatier, and M. J. Bissell, *The Embryonic Environment Strongly Attenuates V-src Oncogenesis in Mesenchymal and Epithelial Tissues but Not in Endothelia*, *J. Cell Biol.* **111**, 217 (1990).
- [71] N. F. Boyd, H. Guo, L. J. Martin, L. Sun, J. Stone, E. Fishell, R. A. Jong, G. Hislop, A. Chiarelli, S. Minkin, and M. J. Yaffe, *Mammographic Density and the Risk and Detection of Breast Cancer*, *N. Engl. J. Med.* **356**, 227 (2007).
- [72] E. A. Sickles, *Wolfe Mammographic Parenchymal Patterns and Breast Cancer Risk*, *Am. J. Roentgenol.* **188**, 301 (2007).
- [73] J. N. Wolfe, *Risk for Breast Cancer Development Determined by Mammographic Parenchymal Pattern*, *Cancer* **37**, 2486 (1976).
- [74] N. Ferrara, K. J. Hillan, H.-P. Gerber, and W. Novotny, *Discovery and Development of Bevacizumab, an Anti-VEGF Antibody for Treating Cancer*, *Nat. Rev. Drug Disc.* **3**, 391 (2004).
- [75] B. Alberts, D. Bray, K. Hopkin, A. D. Johnson, J. Lewis, M. Raff, K. Roberts, and P. Walter, *Essential Cell Biology* (Garland Science, New York, 2013).
- [76] B. Ladoux and R.-M. Mège, *Mechanobiology of Collective Cell Behaviours*, *Nat. Rev. Mol. Cell Biol.* **18**, 743 (2017).
- [77] E. Karsenti and F. Nédélec, *The Mitotic Spindle and Actin Tails*, *Biol. Cell* **96**, 237 (2004).
- [78] S. Petry, A. C. Groen, K. Ishihara, T. J. Mitchison, and R. D. Vale, *Branching Microtubule Nucleation in Xenopus Egg Extracts Mediated by Augmin and TPX2*, *Cell* **152**, 768 (2013).
- [79] J. Zhu, A. Burakov, V. Rodionov, and A. Mogilner, *Finding the Cell Center by a Balance of Dynein and Myosin Pulling and Microtubule Pushing: A Computational Study*, *Mol. Biol. Cell* **21**, 4418 (2010).
- [80] N. Pavin, L. Laan, R. Ma, M. Dogterom, and F. Jülicher, *Positioning of Microtubule Organizing Centers by Cortical Pushing and Pulling Forces*, *New J. Phys.* **14**, 105025 (2012).
- [81] N. Minc, D. Burgess, and F. Chang, *Influence of Cell Geometry on Division-Plane Positioning*, *Cell* **144**, 414 (2011).
- [82] A. Mogilner and E. Craig, *Towards a Quantitative Understanding of Mitotic Spindle Assembly and Mechanics*, *J. Cell Sci.* **123**, 3435 (2010).
- [83] M. I. Molodtsov, C. Mieck, J. Dobbelaere, A. Dammermann, S. Westermann, and A. Vaziri, *A Force-Induced Directional Switch of a Molecular Motor Enables Parallel Microtubule Bundle Formation*, *Cell* **167**, 539 (2016).
- [84] S. Dumont and T. J. Mitchison, *Force and Length in the Mitotic Spindle*, *Curr. Biol.* **19**, R749 (2009).
- [85] G. Civelekoglu-Scholey, D. Sharp, A. Mogilner, and J. Scholey, *Model of Chromosome Motility in Drosophila Embryos: Adaptation of a General Mechanism for Rapid Mitosis*, *Biophys. J.* **90**, 3966 (2006).
- [86] I. M. Tolić-Nørrelykke, *Push-Me-Pull-You: How Microtubules Organize the Cell Interior*, *Eur. Biophys. J.* **37**, 1271 (2008).
- [87] F. Gittes, B. Mickey, J. Nettleton, and J. Howard, *Flexural Rigidity of Microtubules and Actin Filaments Measured from Thermal Fluctuations in Shape*, *J. Cell Biol.* **120**, 923 (1993).
- [88] T. E. Holy, M. Dogterom, B. Yurke, and S. Leibler, *Assembly and Positioning of Microtubule Asters in Microfabricated Chambers*, *Proc. Natl. Acad. Sci. U.S.A.* **94**, 6228 (1997).
- [89] L. Laan, N. Pavin, J. Husson, G. Romet-Lemonne, M. Van Duijn, M. P. López, R. D. Vale, F. Jülicher, S. L. Reck-Peterson, and M. Dogterom, *Cortical Dynein Controls Microtubule Dynamics to Generate Pulling Forces that Position Microtubule Asters*, *Cell* **148**, 502 (2012).
- [90] C. Kozłowski, M. Srayko, and F. Nédélec, *Cortical Microtubule Contacts Position the Spindle in C. elegans Embryos*, *Cell* **129**, 499 (2007).
- [91] P. Gönczy, S. Pichler, M. Kirkham, and A. A. Hyman, *Cytoplasmic Dynein Is Required for Distinct Aspects of MTOC Positioning Including Centrosome Separation, in the One Cell Stage Caenorhabditis Elegans Embryo*, *J. Cell Biol.* **147**, 135 (1999).
- [92] E. M. Gusnowski and M. Srayko, *Visualization of Dynein-Dependent Microtubule Gliding at the Cell Cortex: Implications for Spindle Positioning*, *J. Cell Biol.* **194**, 377 (2011).
- [93] M. Okumura, T. Natsume, M. T. Kanemaki, and T. Kiyomitsu, *Dynein-Dynactin-NuMA Clusters Generate Cortical Spindle-Pulling Forces as a Multi-Arm Ensemble*, *eLife* **7**, e36559 (2018).

- [94] T. Kiyomitsu, *The Cortical Force-Generating Machinery: How Cortical Spindle-Pulling Forces Are Generated*, *Curr. Opin. Cell Biol.* **60**, 1 (2019).
- [95] K. Svoboda and S.M. Block, *Force and Velocity Measured for Single Kinesin Molecules*, *Cell* **77**, 773 (1994).
- [96] S.J. King and T.A. Schroer, *Dynactin Increases the Processivity of the Cytoplasmic Dynein Motor*, *Nat. Cell Biol.* **2**, 20 (2000).
- [97] O. Campas and P. Sens, *Chromosome Oscillations in Mitosis*, *Phys. Rev. Lett.* **97**, 128102 (2006).
- [98] J. Maciejowski, Y. Li, N. Bosco, P.J. Campbell, and T. de Lange, *Chromothripsis and Kataegis Induced by Telomere Crisis*, *Cell* **163**, 1641 (2015).
- [99] N. Tokai-Nishizumi, M. Ohsugi, E. Suzuki, and T. Yamamoto, *The Chromokinesin Kid Is Required for Maintenance of Proper Metaphase Spindle Size*, *Mol. Biol. Cell* **16**, 5455 (2005).
- [100] E. J. Banigan, K. K. Chiou, E. R. Ballister, A. M. Mayo, M. A. Lampson, and A. J. Liu, *Minimal Model for Collective Kinetochore–Microtubule Dynamics*, *Proc. Natl. Acad. Sci. U.S.A.* **112**, 12699 (2015).
- [101] T. S. Hays, D. Wise, and E. Salmon, *Traction Force on a Kinetochore at Metaphase Acts as a Linear Function of Kinetochore Fiber Length*, *J. Cell Biol.* **93**, 374 (1982).
- [102] M. Wühr, E. S. Tan, S. K. Parker, H. W. Detrich, and T. J. Mitchison, *A Model for Cleavage Plane Determination in Early Amphibian and Fish Embryos*, *Curr. Biol.* **20**, 2040 (2010).
- [103] W. Nam and B. I. Epureanu, *Highly Loaded Behavior of Kinesins Increases the Robustness of Transport under High Resisting Loads*, *PLoS Comput. Biol.* **11**, e1003981 (2015).
- [104] S. P. Gross, M. A. Welte, S. M. Block, and E. F. Wieschaus, *Dynein-Mediated Cargo Transport in vivo: A Switch Controls Travel Distance*, *J. Cell Biol.* **148**, 945 (2000).
- [105] V. Mennella, D. A. Agard, B. Huang, and L. Pelletier, *Amorphous No More: Subdiffraction View of the Pericentriolar Material Architecture*, *Trends Cell Biol.* **24**, 188 (2014).
- [106] Y. Bobinnec, A. Khodjakov, L. Mir, C. Rieder, B. Edde, and M. Bornens, *Centriole Disassembly in vivo and Its Effect on Centrosome Structure and Function in Vertebrate Cells*, *J. Cell Biol.* **143**, 1575 (1998).
- [107] M. Abal, G. Keryer, and M. Bornens, *Centrioles Resist Forces Applied on Centrosomes During G2/M Transition*, *Biol. Cell* **97**, 425 (2005).
- [108] M.-F. B. Tsou and T. Stearns, *Mechanism Limiting Centrosome Duplication to Once per Cell Cycle*, *Nature (London)* **442**, 947 (2006).
- [109] M.-F. B. Tsou, W.-J. Wang, K. A. George, K. Uryu, T. Stearns, and P. V. Jallepalli, *Polo Kinase and Separase Regulate the Mitotic Licensing of Centriole Duplication in Human Cells*, *Dev. Cell* **17**, 344 (2009).
- [110] A. Kubo, H. Sasaki, A. Yuba-Kubo, S. Tsukita, and N. Shiina, *Centriolar Satellites Molecular Characterization ATP-Dependent Movement Toward Centrioles and Possible Involvement in Ciliogenesis*, *J. Cell Biol.* **147**, 969 (1999).
- [111] F. Bärenz, D. Mayilo, and O. J. Gruss, *Centriolar Satellites: Busy Orbits around the Centrosome*, *Eur. J. Cell Biol.* **90**, 983 (2011).
- [112] A. Dammermann and A. Merdes, *Assembly of Centrosomal Proteins and Microtubule Organization Depends on PCM-1*, *J. Cell Biol.* **159**, 255 (2002).
- [113] M. M. Mogensen, A. Malik, M. Piel, V. Bouckson-Castaing, and M. Bornens, *Microtubule Minus-End Anchorage at Centrosomal and Non-centrosomal Sites: The Role of Ninein*, *J. Cell Sci.* **113**, 3013 (2000).
- [114] N. Delgehr, J. Sillibourne, and M. Bornens, *Microtubule Nucleation and Anchoring at the Centrosome Are Independent Processes Linked by Ninein Function*, *J. Cell Sci.* **118**, 1565 (2005).
- [115] B. Leber, B. Maier, F. Fuchs, J. Chi, P. Riffel, S. Anderhub, L. Wagner, A. D. Ho, J. L. Salisbury, M. Boutros *et al.*, *Proteins Required for Centrosome Clustering in Cancer Cells*, *Sci. Transl. Med.* **2**, 33ra38 (2010).
- [116] S. W. Krauss, J. R. Spence, S. Bahmanyar, A. I. Barth, M. M. Go, D. Czerwinski, and A. J. Meyer, *Downregulation of Protein 4.1R, a Mature Centriole Protein, Disrupts Centrosomes, Alters Cell Cycle Progression, and Perturbs Mitotic Spindles and Anaphase*, *Mol. Cell Biol.* **28**, 2283 (2008).
- [117] E. Logarinho, S. Maffini, M. Barisic, A. Marques, A. Toso, P. Meraldi, and H. Maiato, *CLASPs Prevent Irreversible Multipolarity by Ensuring Spindle-Pole Resistance to Traction Forces During Chromosome Alignment*, *Nat. Cell Biol.* **14**, 295 (2012).
- [118] M. Kimura, T. Yoshioka, M. Saio, Y. Banno, H. Nagaoka, and Y. Okano, *Mitotic Catastrophe and Cell Death Induced by Depletion of Centrosomal Proteins*, *Cell Death Disease* **4**, e603 (2013).
- [119] K. Kim and K. Rhee, *The Pericentriolar Satellite Protein CEP90 Is Crucial for Integrity of the Mitotic Spindle Pole*, *J. Cell Sci.* **124**, 338 (2011).
- [120] N. Oshimori, X. Li, M. Ohsugi, and T. Yamamoto, *CEP72 Regulates the Localization of Key Centrosomal Proteins and Proper Bipolar Spindle Formation*, *EMBO J.* **28**, 2066 (2009).
- [121] J.-H. Sir, A. R. Barr, A. K. Nicholas, O. P. Carvalho, M. Khurshid, A. Sossick, S. Reichelt, C. D'Santos, C. G. Woods, and F. Gergely, *A Primary Microcephaly Protein Complex Forms a Ring around Parental Centrioles*, *Nat. Genetics* **43**, 1147 (2011).
- [122] A. R. Barr, J. V. Kilmartin, and F. Gergely, *CDK5RAP2 Functions in Centrosome to Spindle Pole Attachment and DNA Damage Response*, *J. Cell Biol.* **189**, 23 (2010).
- [123] J. A. Barrera, L.-R. Kao, R. E. Hammer, J. Seemann, J. L. Fuchs, and T. L. Megraw, *CDK5RAP2 Regulates Centriole Engagement and Cohesion in Mice*, *Dev. Cell* **18**, 913 (2010).
- [124] V. Marthiens, M. Piel, and R. Basto, *Never Tear Us Apart—The Importance of Centrosome Clustering*, *J. Cell Sci.* **125**, 3281 (2012).
- [125] F. Verde, M. Dogterom, E. Stelzer, E. Karsenti, and S. Leibler, *Control of Microtubule Dynamics and Length by Cyclin A- and Cyclin B-dependent Kinases in Xenopus Egg Extracts*, *J. Cell Biol.* **118**, 1097 (1992).

- [126] S. Inoué and E. D. Salmon, *Force Generation by Microtubule Assembly/Disassembly in Mitosis and Related Movements*, *Mol. Biol. Cell* **6**, 1619 (1995).
- [127] L. Gombos, A. Neuner, M. Berynskyy, L. L. Fava, R. C. Wade, C. Sachse, and E. Schiebel, *GTP Regulates the Microtubule Nucleation Activity of γ -Tubulin*, *Nat. Cell Biol.* **15**, 1317 (2013).
- [128] G. Goshima, F. Nédélec, and R. D. Vale, *Mechanisms for Focusing Mitotic Spindle Poles by Minus End-Directed Motor Proteins*, *J. Cell Biol.* **171**, 229 (2005).
- [129] M. Dogterom and B. Yurke, *Measurement of the Force-Velocity Relation for Growing Microtubules*, *Science* **278**, 856 (1997).
- [130] A. Burakov, E. Nadezhkina, B. Slepchenko, and V. Rodionov, *Centrosome Positioning in Interphase Cells*, *J. Cell Biol.* **162**, 963 (2003).
- [131] R. Wollman, E. Cytrynbaum, J. Jones, T. Meyer, J. M. Scholey, and A. Mogilner, *Efficient Chromosome Capture Requires a Bias in the Search-and-Capture Process During Mitotic-Spindle Assembly*, *Curr. Biol.* **15**, 828 (2005).
- [132] R. Loughlin, R. Heald, and F. Nédélec, *A Computational Model Predicts Xenopus Meiotic Spindle Organization*, *J. Cell Biol.* **191**, 1239 (2010).
- [133] F. Nédélec, *Computer Simulations Reveal Motor Properties Generating Stable Antiparallel Microtubule Interactions*, *J. Cell Biol.* **158**, 1005 (2002).
- [134] Z. Wang, S. Khan, and M. P. Sheetz, *Single Cytoplasmic Dynein Molecule Movements: Characterization and Comparison with Kinesin*, *Biophys. J.* **69**, 2011 (1995).
- [135] T. Gao, R. Blackwell, M. A. Glaser, M. Betterton, and M. J. Shelley, *Multiscale Polar Theory of Microtubule and Motor-Protein Assemblies*, *Phys. Rev. Lett.* **114**, 048101 (2015).
- [136] C. Faivre-Moskalenko and M. Dogterom, *Dynamics of Microtubule Asters in Microfabricated Chambers: The Role of Catastrophes*, *Proc. Natl. Acad. Sci. U.S.A.* **99**, 16788 (2002).
- [137] A. Gennerich, A. P. Carter, S. L. Reck-Peterson, and R. D. Vale, *Force-Induced Bidirectional Stepping of Cytoplasmic Dynein*, *Cell* **131**, 952 (2007).